FILE COPY

TECHNICAL REPORT BRL-TR-3273

BRL

PENETRATION OF SHAPED-CHARGE JETS INTO GLASS AND CRYSTALLINE QUARTZ

G. E. HAUVER
P. H. NETHERWOOD
R. F. BENCK
A. MELANI

SEPTEMBER 1991

U.S. ARMY LABORATORY COMMAND

BALLISTIC RESEARCH LABORATORY
ABERDEEN PROVING GROUND, MARYLAND

NOTICES

REPORT DOCUMENTATION PAGE	Form Approved OMB No 0/04 0188

1. AGENCY USE ONLY (leave blank)	2. REPORT DATE September 1991	3. REPORT TYPE AND DATES COVERED Final, January 1984–January 1989

4. TITLE AND SUBTITLE	5. FUNDING NUMBERS
Penetration of Shaped-Charge Jets Into Glass and Crystalline Quartz	
6. AUTHOR(S) G. E. Hauver, P. H. Netherwood, R. F. Benck, and A. Melani	1L161102AH43

7. PERFORMING ORGANIZATION NAME(S) AND ADDRESS(ES)	8. PERFORMING ORGANIZATION REPORT NUMBER
Director U.S. Army Ballistic Research Laboratory ATTN: SLCBR-TB-AM Aberdeen Proving Ground, MD 21005-5066	

9. SPONSORING/MONITORING AGENCY NAME(S) AND ADDRESS(ES)	10. SPONSORING/MONITORING AGENCY REPORT NUMBER
U.S. Army Ballistic Research Laboratory ATTN: SLCBR-DD-T Aberdeen Proving Ground, MD 21005-5066	BRL–TR–3273

11. SUPPLEMENTARY NOTES

12a. DISTRIBUTION/AVAILABILITY STATEMENT	12b. DISTRIBUTION CODE
Approved for public release; distribution is unlimited.	

13. ABSTRACT (Maximum 200 words)

Penetration of shaped charge jets into glass and crystalline quartz was studied by high-speed photography and flash radiography to identify behavior responsible for the effectiveness of glass against shaped charge threats. The behavior of crystalline quartz was relatively conventional. The greater effectiveness of silica and high-silica glasses was clearly indicated by an abrupt decrease in penetration velocity shortly after impact. High-speed photographs showed that the penetration path opened to its maximum diameter within a few microseconds and then rapidly closed after the penetration front passed. The penetration velocity decreased when jet elements, disturbed by cavity closure, arrived at the penetration front. The penetration path in recovered targets was filled with a red copper-glass that resulted from an extended interaction between jet and target materials. Closure preceded brittle failure in the surrounding glass target, and it was concluded that primary closure is caused by recovery from high pressures near the penetration front.

14. SUBJECT TERMS			15. NUMBER OF PAGES 59
penetration; jets; shaped-charge jets; glass; quartz; cavity closure			16. PRICE CODE

17. SECURITY CLASSIFICATION OF REPORT	18. SECURITY CLASSIFICATION OF THIS PAGE	19. SECURITY CLASSIFICATION OF ABSTRACT	20. LIMITATION OF ABSTRACT
UNCLASSIFIED	UNCLASSIFIED	UNCLASSIFIED	SAR

INTENTIONALLY LEFT BLANK.

TABLE OF CONTENTS

INTENTIONALLY LEFT BLANK.

LIST OF FIGURES

ACKNOWLEDGMENT

Intentionally left blank.

1. INTRODUCTION

Experiments performed at the Carnegie Institute of Technology (CIT) during World War II showed that glass has an unusual ability to resist penetration by shaped charge jets. After World War II, Pugh and his associates at CIT studied the performance of glass targets and established general principles (Heine-Geldern 1954; Allison 1960) that apply to the use of glass for shaped charge protection. However, the physical behavior underlying these principles remained obscure. The studies described in this report were undertaken to identify dynamic behavior responsible for the effectiveness of glass targets.

As an introduction to the recent studies, it may be useful to examine Figure 1, which is a photograph from a 1955 publication (Zernow and Hauver 1955). This back-lighted photograph shows an unconfined glass target as it is penetrated by a small copper jet. The most prominent features in the photograph are (A) the central dark region, (B) the dark envelope that resembles a bow wave, (C) the envelope of trailing fracture, and (D) the impact shock which is still visible at the lower extremes. The central dark region was assumed to define the penetration path. The penetration velocity of the jet in Figure 1 is subsonic, so the only shock wave is the one produced at impact. Consequently, the envelope that resembles a bow wave must have another origin. Earlier Kerr-Cell photographs at CIT (Pugh et al. 1951) clearly showed that this envelope encloses a cylindrical volume around the penetration path in soda-lime glass.

Concurrent with the CIT investigations, Bridgman and Simon (1953) discovered that fused quartz and other glasses become permanently densified under static compression at high pressure. Since that time, many studies of permanent densification under static and dynamic compression have been conducted, including Viard (1959), Wackerle (1962), Cohen and Roy (1965), Arndt, Hornemann, and Muller (1971), Gibbons and Ahrens (1971), Anan'in et al. (1974a), Kanel, Molodets, and Dremin (1976), Cagnoux (1981), and Sugiura, Kondo, and Sawaoka (1981) which are considered most pertinent to the present investigation. In the present investigation, particles ejected from a fused quartz target during jet penetration were found to be permanently densified by up to 10%. This observation supports the assumption that the envelope surrounding the penetration path is a boundary between glass which is

1
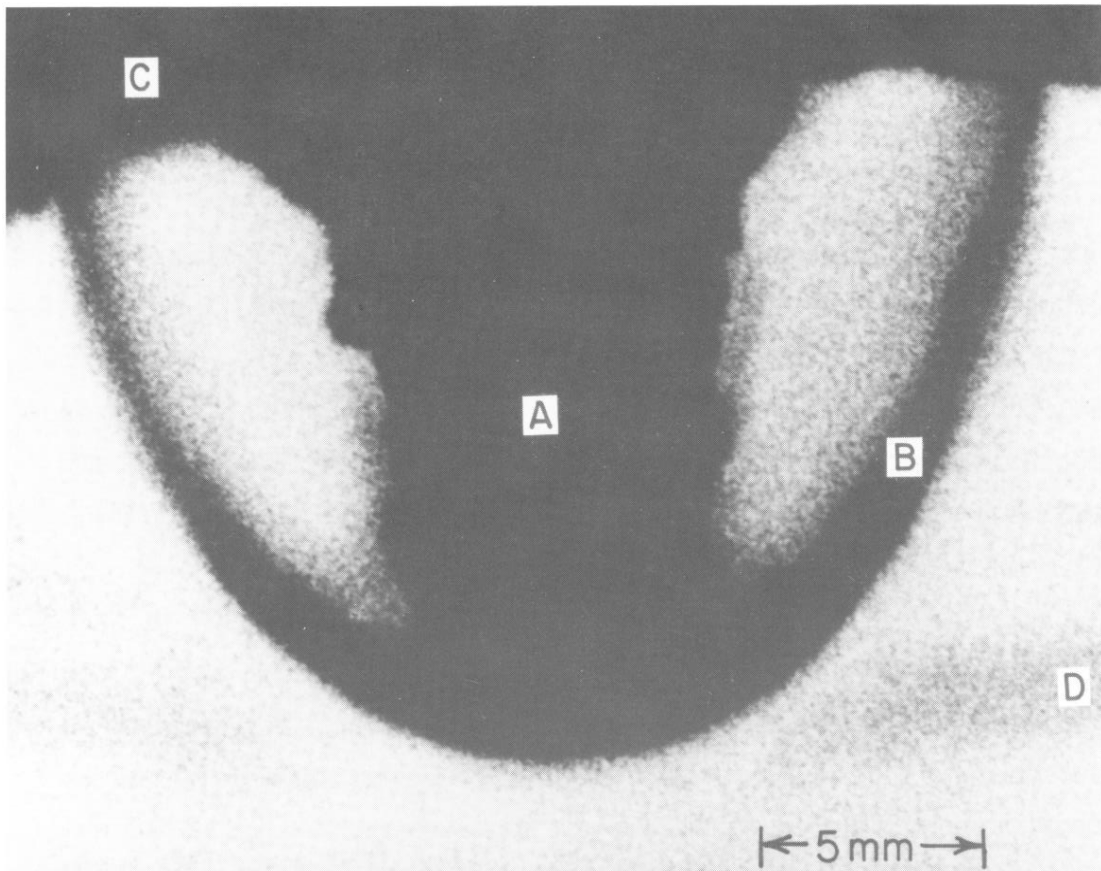
Figure 1. <u>Photograph of a Glass Target During Penetration by a Shaped Charge Jet</u>.

elastically deformed and glass which has yielded to become permanently densified. In Figure 1, permanently densified glass resides between the envelope (B) and the penetration path (A).

Tests were recently conducted with targets of glass and crystalline quartz to obtain further information about jet-target interactions. These tests used flash radiography and high-speed photography to observe behavior during penetration. In the tests that used flash radiography, metallic confinement allowed the targets to be recovered for post-test examinations which further helped to identify behavior. These recent tests will be described and discussed in the following sections of the report.

2. EXPERIMENTS AND DISCUSSION

2.1 <u>Test Charge</u>. Most of the penetration experiments were conducted with the jet from a shaped charge liner with a base diameter of 35 mm. This liner was obtained by reducing the

base diameter of an obsolete M9A1 copper cone which had an apex angle of 42° and a nominal wall thickness of 0.89 mm. The explosive was unconfined Composition B (diameter = 35 mm) which extended to 1.5 times the cone height. This explosive was initiated by a PBX booster (diameter = 19 mm; height = 13 mm) in combination with an M18 detonator. An earlier study (Hauver and Benson 1955) showed that an M18 improves the axial symmetry of a detonation wave, mainly by restricting the area over which the booster is initiated. The primary detonator contained PETN powder which was initiated by an exploding bridgewire. The velocity of the jet tip was approximately 7,830 m/s, and during free flight, breakup occurred approximately 20.7 µs after the jet emerged from the base of the liner, producing particles with an average length of 2.6 mm (Franz and Lawrence 1987).

2.2 Examination of Penetration-Time Data. Data for depth of penetration as a function of time were always examined with the aid of a Modified Bernoulli Model (Tate 1967, 1969), assuming a virtual origin and a linear distribution of velocity along the jet. The jet was assumed to elongate until the breakup time determined experimentally during free flight in air. At breakup, the jet was subdivided into segments with the average length determined experimentally. During free flight, segments were assumed to maintain both their assigned length and their axial alignment. In metallic targets, the target-strength term in the model is defined as the quasi-static pressure, R, required to open a spherical cavity from zero initial radius. In applying the model to glass targets, R was considered only as a measure of resistance to penetration, and it served as a fitting parameter. In this method of application, values for R were clearly dependent not only on the target material, but also on jet behavior and details of the jet-target interaction. Basically, the simple model has no realistic means for treating the complexity of penetration in a glass target. Despite a loss of fundamental significance, values of R were useful for comparing one test with another, and for locating changes in penetration behavior during a single test. Reasons for changes in the value of R were then subject to interpretation based on experimental evidence. The stress unit is included with R values cited in the text, as a formality, but it is omitted in figures where relative magnitudes of R are of primary interest.

2.3 Flash-Radiographic Observations During Jet Penetration. Jet penetration into targets of fused quartz and crystalline quartz was observed by 450-kV flash radiography. Targets for the flash-radiographic tests are shown in Figure 2. Although target configurations (A) and (B)

3
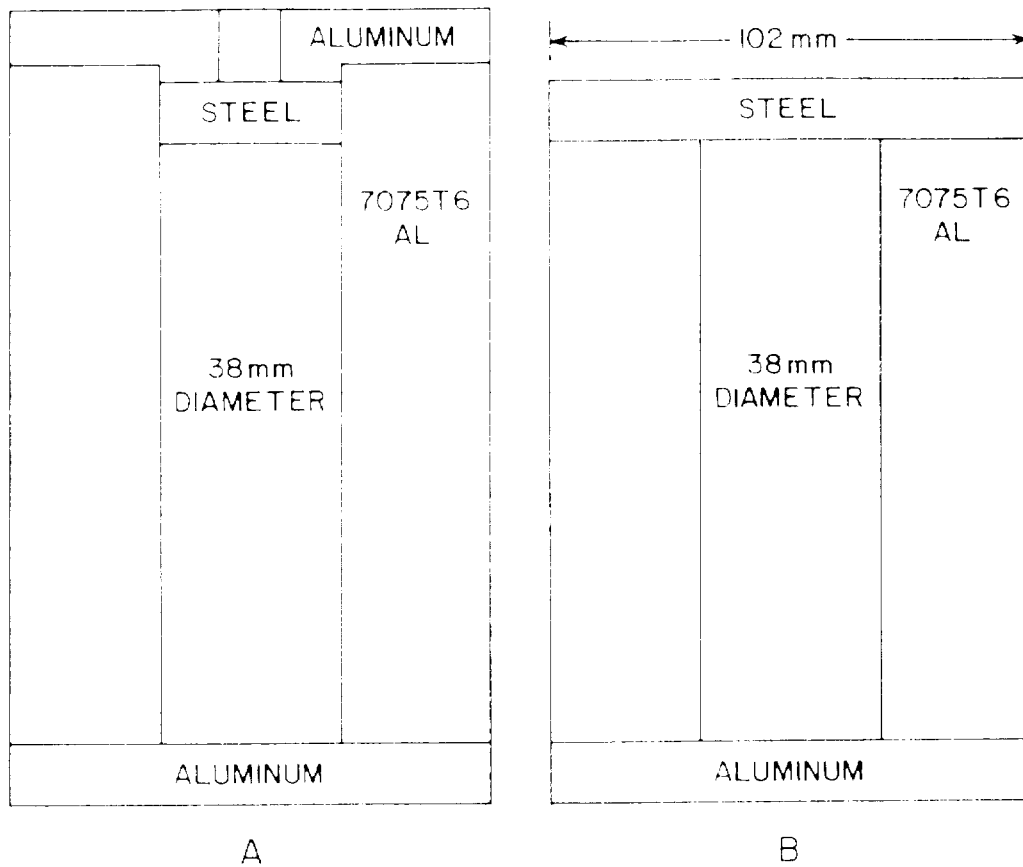
Figure 2. Target Configurations for Radiographic Tests.

were both used for tests with fused quartz, only configuration (A) was used for tests with crystalline quartz. The small size of the jet (1.0 1.5 mm diameter), the material of the jet (copper), the relatively large x ray source size (5.0 mm diameter), and scattered radiation contributed to imaging problems, and little detail could be discerned before tracer material was introduced into targets. Different tracer materials and configurations were tested, and radiographs of jet penetration into targets containing tracers are shown in Figure 3.

The target material in Figure 3A is fused quartz with a density of 2.20 Mg/m³, and the tracer material is lead glass. Penetration has proceeded from top to bottom in the figure. Although penetration has advanced beyond the lower tracer, details near the penetration front are not well defined and the jet can be resolved only above the upper tracer where it is clearly disrupted. Tracer material has flowed into the target (toward the bottom of the figure) and defines portions of the penetration path. Displaced tracer material is not concentrated along

4
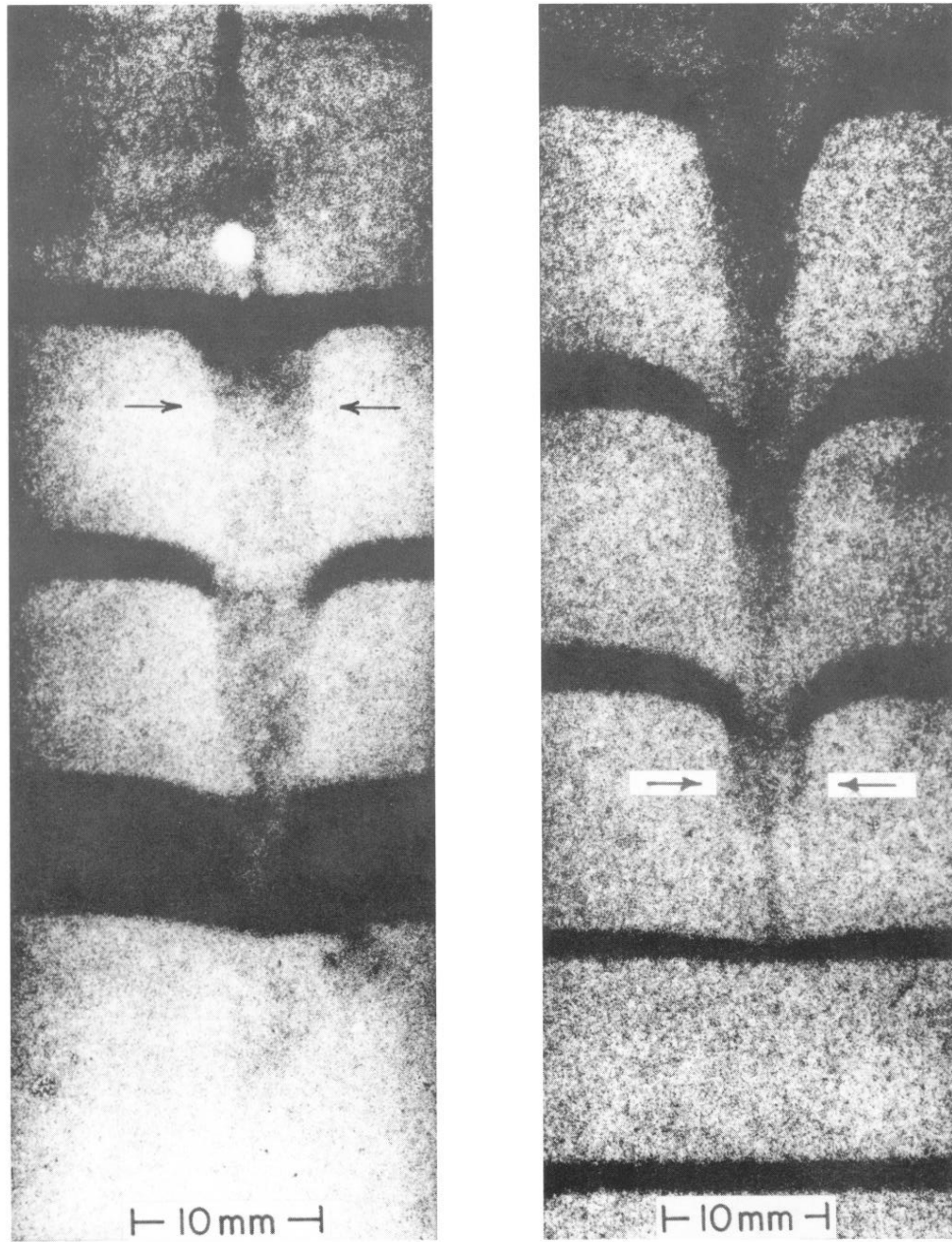
Figure 3. Flash Radiographs Showing Jet Penetration Into (A) Fused Quartz and (B) Crystalline Quartz.

the wall of the penetration path. The arrows in Figure 3A indicate the location of optical density measurements across the image of the penetration path, and Figure 4A shows the density change, ΔD, as a function of distance. A uniform distribution of absorbing material within the path would be expected to produce the dashed profile. The measured profile is similar, but asymmetry is present and is probably caused by displaced jet material. The displaced jet material is seen above the upper tracer, and its location is in qualitative agreement with the asymmetry, although the jet cannot be resolved at the location of density measurements. The penetration path between the two upper tracers has a diameter of approximately 5 mm, which was confirmed when the recovered target was sectioned and measured.

The target in Figure 3B is polycrystalline quartz with a density of 2.64 Mg/m³, and the tracer material is tantalum carbide ceramic. Lead glass tracers were not used in order to avoid any misinterpretation that might result from behavior characteristic of glass. Penetration into crystalline quartz appears to be more conventional than penetration into fused quartz. The jet can be distinguished at the penetration front and material displaced from the central tracer appears to be concentrated along the cavity wall. The arrows in Figure 3B indicate the location of optical density measurements across the penetration path, and Figure 4B shows the density change, ΔD, as a function of distance. The dashed curve in Figure 4B depicts an idealized density profile that would be expected if absorbing material were confined to a rod with a diameter of 1.2 mm and a tube with an outside diameter of 4.96 mm and a wall thickness of 1.15 mm. The measured density profile is similar to the idealized one, but asymmetry is present. In this case, the jet is observed to be slightly off axis at the measurement location, and this produces some merging of tube and jet profiles at the left side. The flash radiograph in Figure 3B does not provide clear evidence of cavity closure during penetration, although closure was found in the recovered target.

The locations for density scans in Figures 3 and 4 were not arbitrarily selected. They were selected to illustrate most clearly the qualitative observations about distributions of jet and target material within penetration paths in fused quartz and crystalline quartz. In the case of fused quartz, the most suitable location was between the upper two tracers. Because of

6
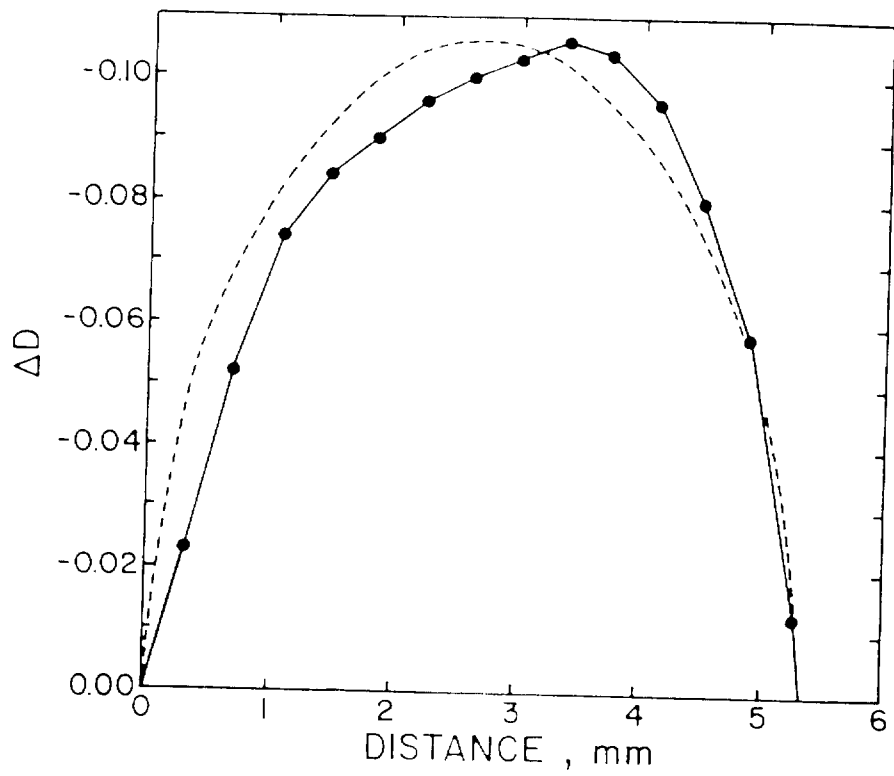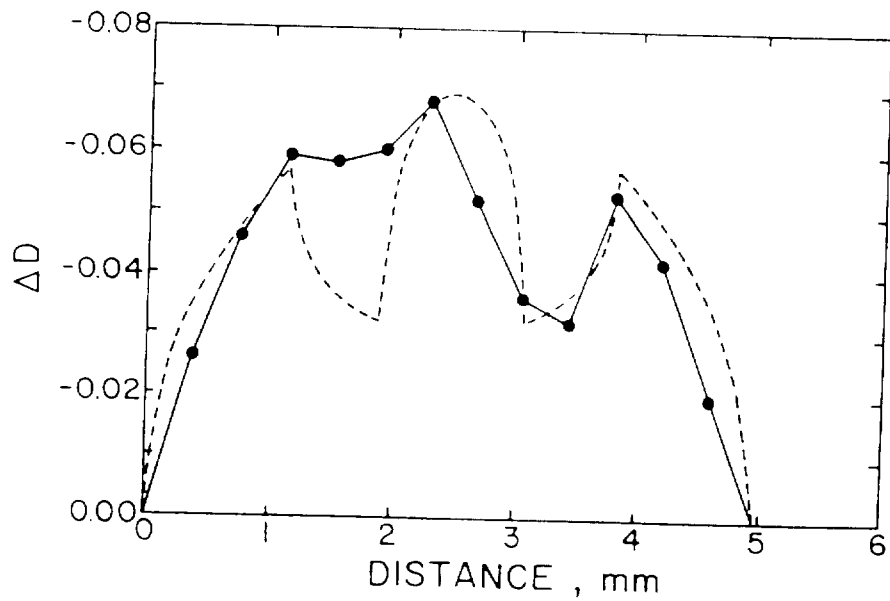
Figure 4. Profiles of Optical Density Across Penetration Paths in (A) Fused Quartz and (B) Crystalline Quartz.

low image contrast, a location closer to the upper tracer provided a higher concentration of tracer material and improved the contrast for measurements. In the case of crystalline quartz, the critical location was between the central tracer and the next lower tracer. Qualitatively, the jet was visible (in the original radiograph) within this entire region. However, tracer material was more concentrated close to the central tracer, so the density scan was conducted at this location where it could benefit from improved image contrast.

Strain fields are observed to be different in the fused quartz and crystalline quartz targets shown in Figure 3. In fused quartz, displacement at the bottom surface of tracers defines a column with a diameter of 9-10 mm which, in high-silica glasses, corresponds closely to the diameter of the envelope containing permanently densified material. In crystalline quartz, displaced material at the bottom surface of tracers defines a column with a larger diameter of 15-16 mm. It is assumed that large displacements in crystalline quartz were associated with failure into particles or microblocks (Anan'in et al. 1974b) which were subsequently displaced. Displaced particles should not fit together compactly, and this represents a source of dilatancy that might produce cavity closure. However, Figure 3B suggests that cavity closure in crystalline quartz does not proceed rapidly since there is no clear evidence of closure at this stage of the penetration.

2.4 Photographic Measurements of Penetration Time. Jet penetration into glass was observed by high-speed photography in an effort to examine the penetration path near the penetration front where flash radiographs did not provide well-defined features in fused quartz. The initial photographic studies were conducted with blocks of fused quartz, but later studies used targets of commercial soda-lime glass. The blocks of fused quartz offered good optical quality and no interfaces where failure could be initiated by the impact shock. However, fracture propagated at a velocity nearly equal to the penetration velocity in fused quartz and quickly obscured details near the penetration front, making this material a poor choice for optical studies. Despite this shortcoming, fused quartz was of interest because it has been the subject of many high pressure studies and offers a direct comparison with penetration behavior in crystalline quartz. In later tests with soda-lime glass, the penetration velocity greatly exceeded the fracture velocity during the early part of penetration. Photographs of the exposed penetration path in soda-lime glass provided insight into behavior during jet

8

penetration and made this material more useful for photographic studies, even though thicknesses greater than 25 mm were not readily available.

2.4.1 Experimental Configurations for Photographic Studies. Representative configurations for photographic observations of penetration are shown in Figures 5 and 6. The earliest tests were conducted with back lighting as shown in Figure 5. A plastic Fresnel lens imaged the light from an exploding wire into the aperture of a high-speed framing camera. The target was located close to the Fresnel lens and consisted of a glass block, backed by steel, with a cover of polymethylmethacrylate (PMMA). The PMMA cover was usually 25 mm thick and shielded the glass from debris that might precede the jet. Penetration in the PMMA was supersonic, allowing the jet to arrive at the glass before other disturbances that could produce damage. Targets commonly had a 102-mm-square cross section. Waves reflected from the lateral boundary never produced troublesome surface damage and did not return to the axis of penetration before measurements were completed.
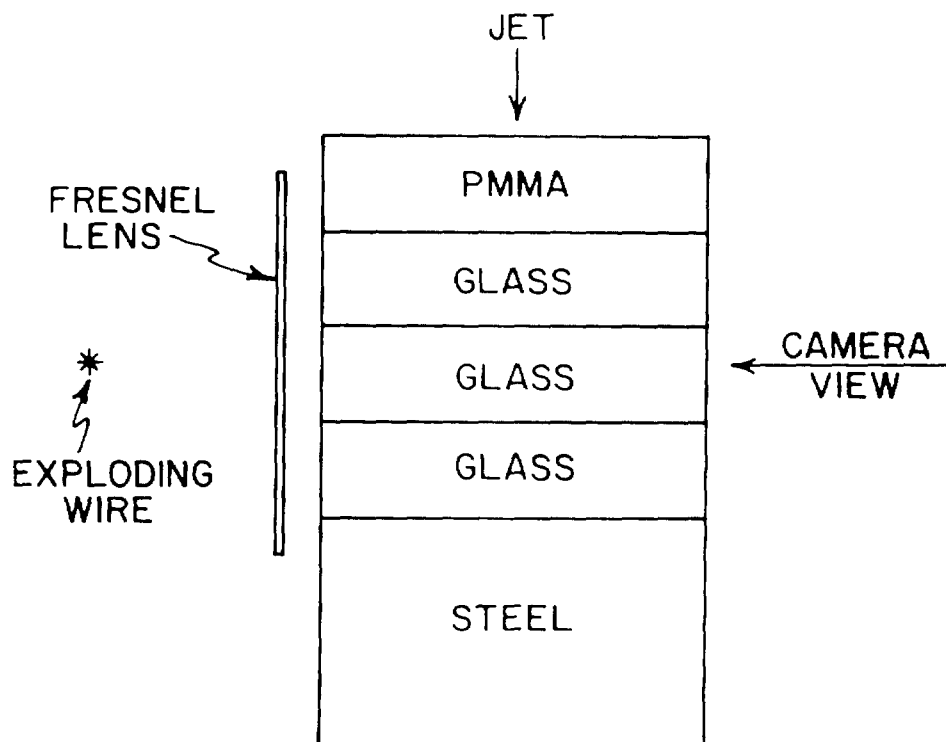
Figure 5. Configuration for Photographic Tests With Back Lighting.

9

JET
AXIS

CAMERA
VIEW

TOP VIEW

OPAQUE
SHIELD

EXPLODING
WIRE

WHITE
REFLECTOR/
DIFFUSER

JET

PMMA

GLASS

GLASS

GLASS

STEEL

SIDE VIEW

SHIELD

CAMERA
VIEW

EXPLODING
WIRE
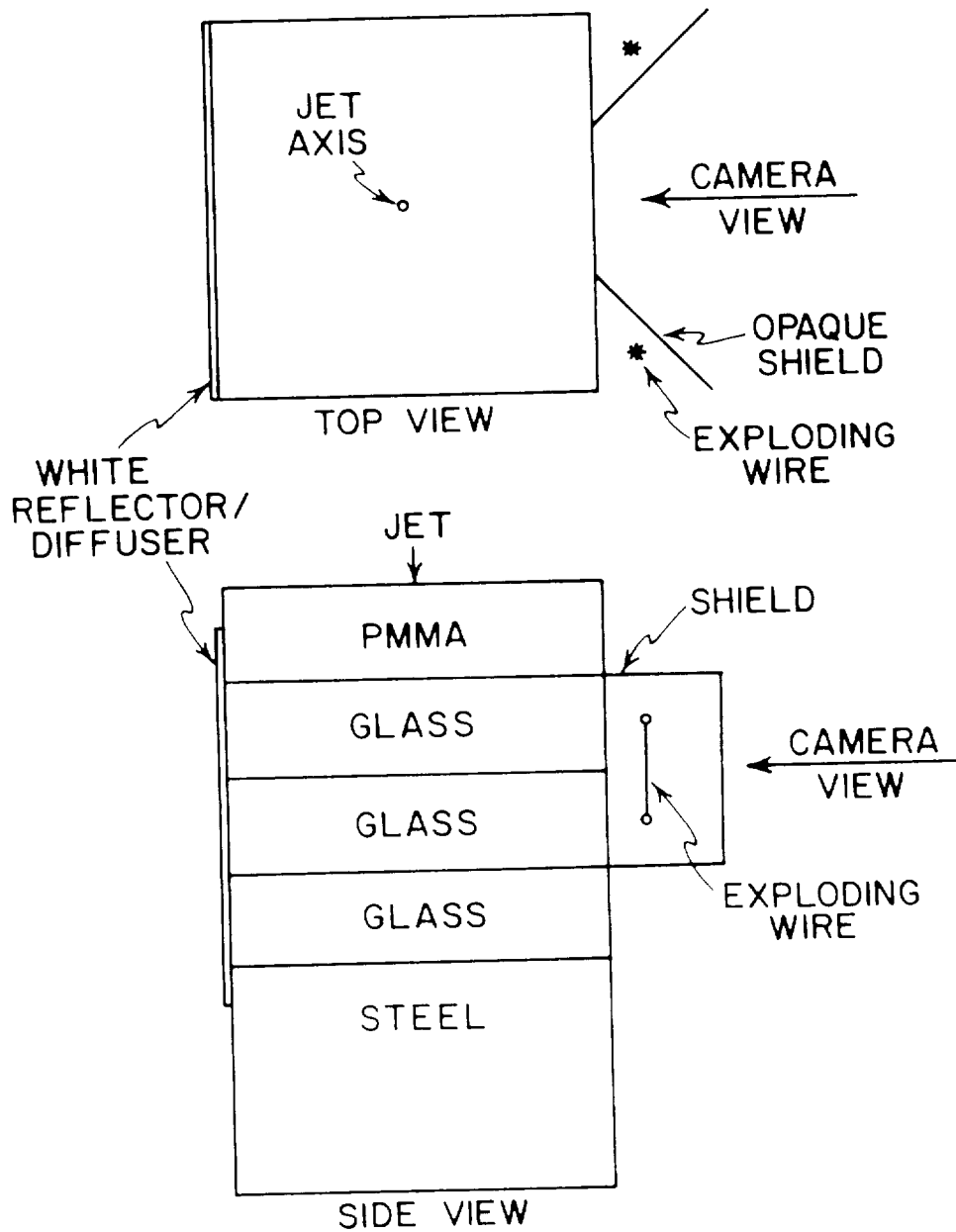
Figure 6. Configuration for Photographic Tests With Front Lighting.

10

Damage that limited photographic observations was characteristically initiated close to the axis of penetration at interfaces or imperfections in the glass. Unfortunately, the permanently densified region around the penetration path strongly refracted the back light and prevented critical observations. Consequently, the front lighted test configuration in Figure 6 was introduced to overcome the refraction problem associated with back lighting. Front lighting was provided by exploding tungsten wires which were shielded from direct observation by the camera. A white card at the back of the target provided weak, diffused back lighting in addition to the strong front lighting, and this combination was judged to provide the most complete photographic detail.

Glass targets were photographed during penetration by both continuous and particulated jets. In all tests to be reported, photographs were taken at 1 µs intervals. When the standoff distance was approximately 140 mm, jet breakup occurred during penetration in the thick PMMA cover and penetration in the glass was entirely by jet segments or particles. When the standoff distance was approximately 50 mm, the jet usually remained continuous throughout all of the observed penetration into glass.

2.4.2 Jet Penetration Into Fused Quartz. Figure 7 shows penetration-time data obtained by high-speed photography during jet penetration into monolithic fused quartz. Jet breakup occurred during penetration in the PMMA cover. The penetration model generated a penetration path in agreement with the experimental data when the assigned target resistance was 11 GPa. After approximately 10 µs of penetration into fused quartz, the experimental data began to deviate slightly from the calculated penetration path. Agreement with the later data points was achieved by assigning a higher resistance value of 22 GPa. Photographic measurements ended at approximately 16.3 µs when the penetration front was overtaken and obscured by trailing fracture.

Flash radiographic tests, reported in Section 2.3, provided a few measurements of the penetration depth in fused quartz after fracture obscured the penetration front and ended photographic measurements. In Figure 8, these radiographic data are combined with the photographic data. The radiographic data on Curve A were obtained from tests with Target A in Figure 2; the one datum point on Curve B was obtained from a test with Target B. For

11

Figure ... Penetration into Fused Quartz
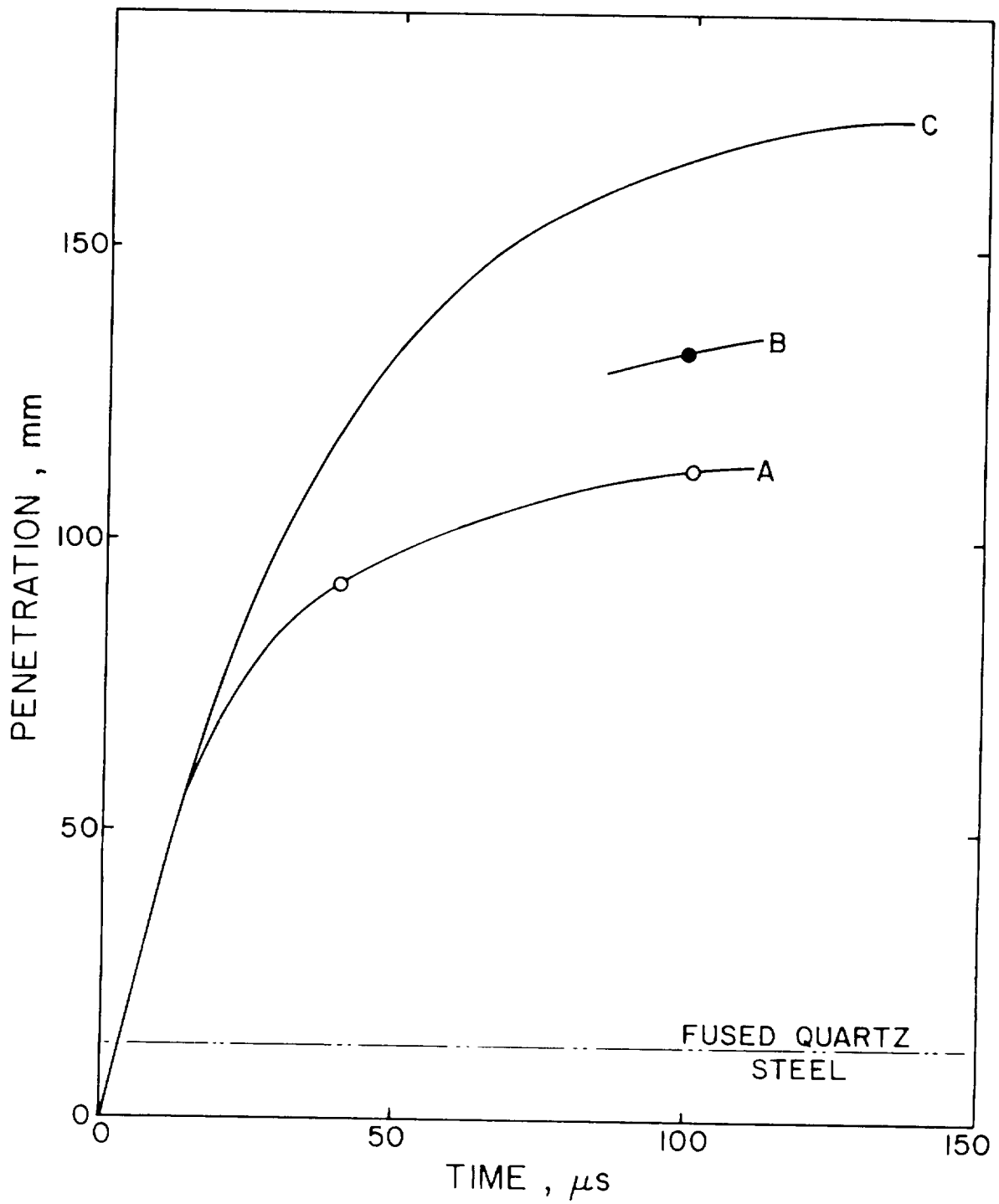
Figure 8. Combined Radiographic and Photographic Data for Jet Penetration Into Fused Quartz.

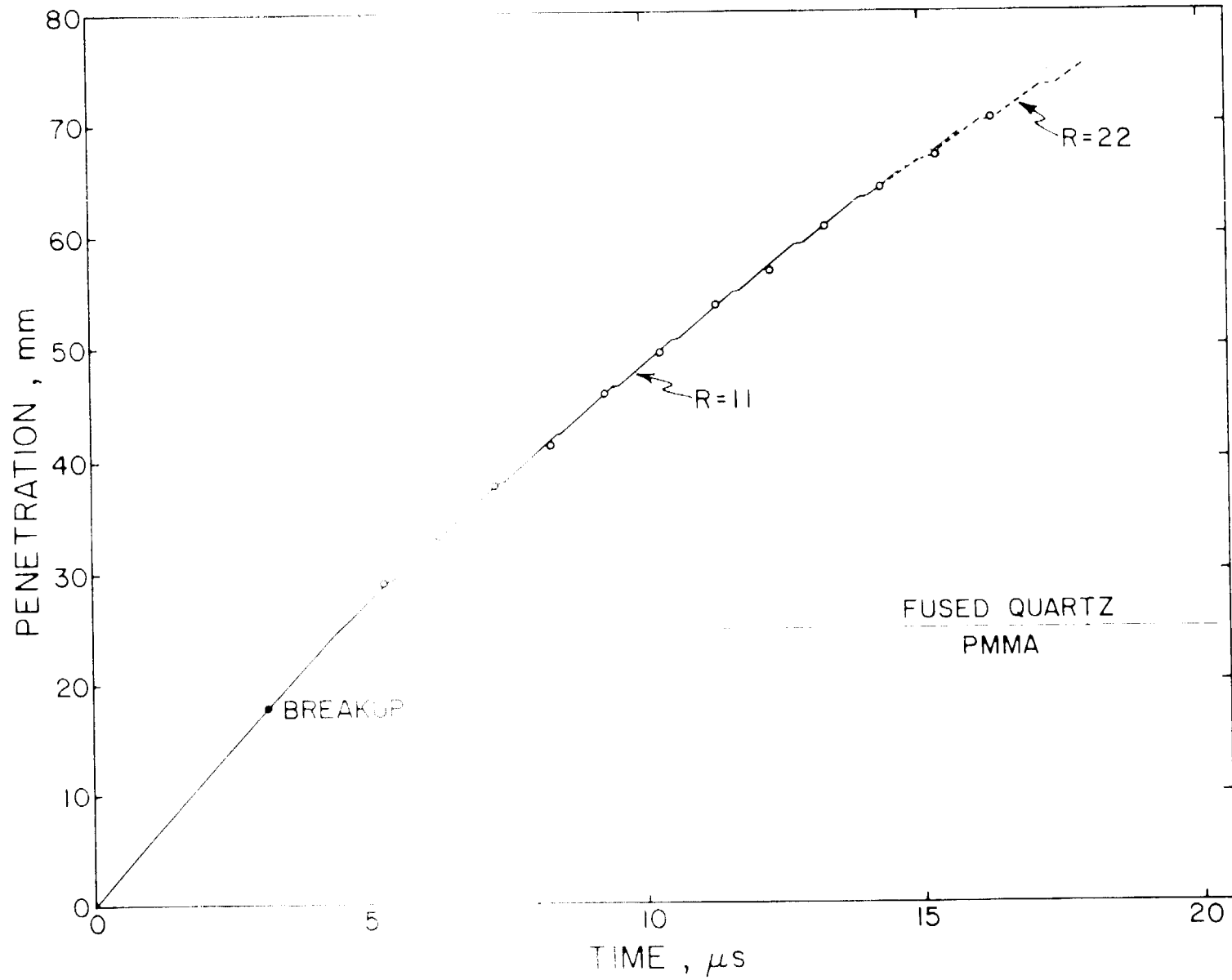reference, Curve C is an extrapolation of data at the beginning of penetration in Figure 7, where the assigned target resistance was 11 GPA. Radiographic data confirmed a substantial increase in target resistance during jet penetration into fused quartz, in agreement with the minimal photographic evidence for such an increase. Target A became more resistant to penetration than Target B. These target configurations provided similar lateral confinement for the fused quartz core, but Target A provided better confinement by the front steel plate. An examination of recovered targets revealed that as the steel plate in Target A was penetrated, radial deformation caused engravement into the surrounding aluminum, keeping it in place. In comparison, the steel plate at the front of Target B bulged outward, reducing the confinement of core material.

In Figure 9, penetration into fused quartz is compared with penetration into crystalline quartz. The curve for fused quartz (FQ) is based on both the photographic data and the radiographic data obtained with Target A. The curve for crystalline quartz (CQ) is based solely on one radiographic measurement with Target A. By assigning crystalline quartz a target resistance of 14 GPa, the model provided close agreement with both the radiographic datum point and the final depth of penetration measured in the recovered target. This agreement suggested that cavity closure, found in the recovered target, did not occur quickly enough to have a significant influence on jet penetration into crystalline quartz. In Figure 9, it is apparent that fused quartz, early in the penetration, becomes a more resistant target material than crystalline quartz.

Although high-speed photography was able to provide penetration-time data for fused quartz, the rapid propagation of trailing fracture always prevented observations of the penetration path in the region behind the penetration front where details were poorly defined in flash radiographs and where information was needed to explain the increase in target resistance during jet penetration. Borosilicate glass allowed more of the penetration path to be observed, but photographs by Zernow and Hauver (1955) and by Pugh et al. (1951) showed a greater length of the penetration path than could be observed with borosilicate glass. The greatest observed path length implies the lowest rate of fracture propagation which would make such a glass most suitable for photographic observations. The glass used by Zernow and Hauver was recently analyzed and identified as a soda-lime composition

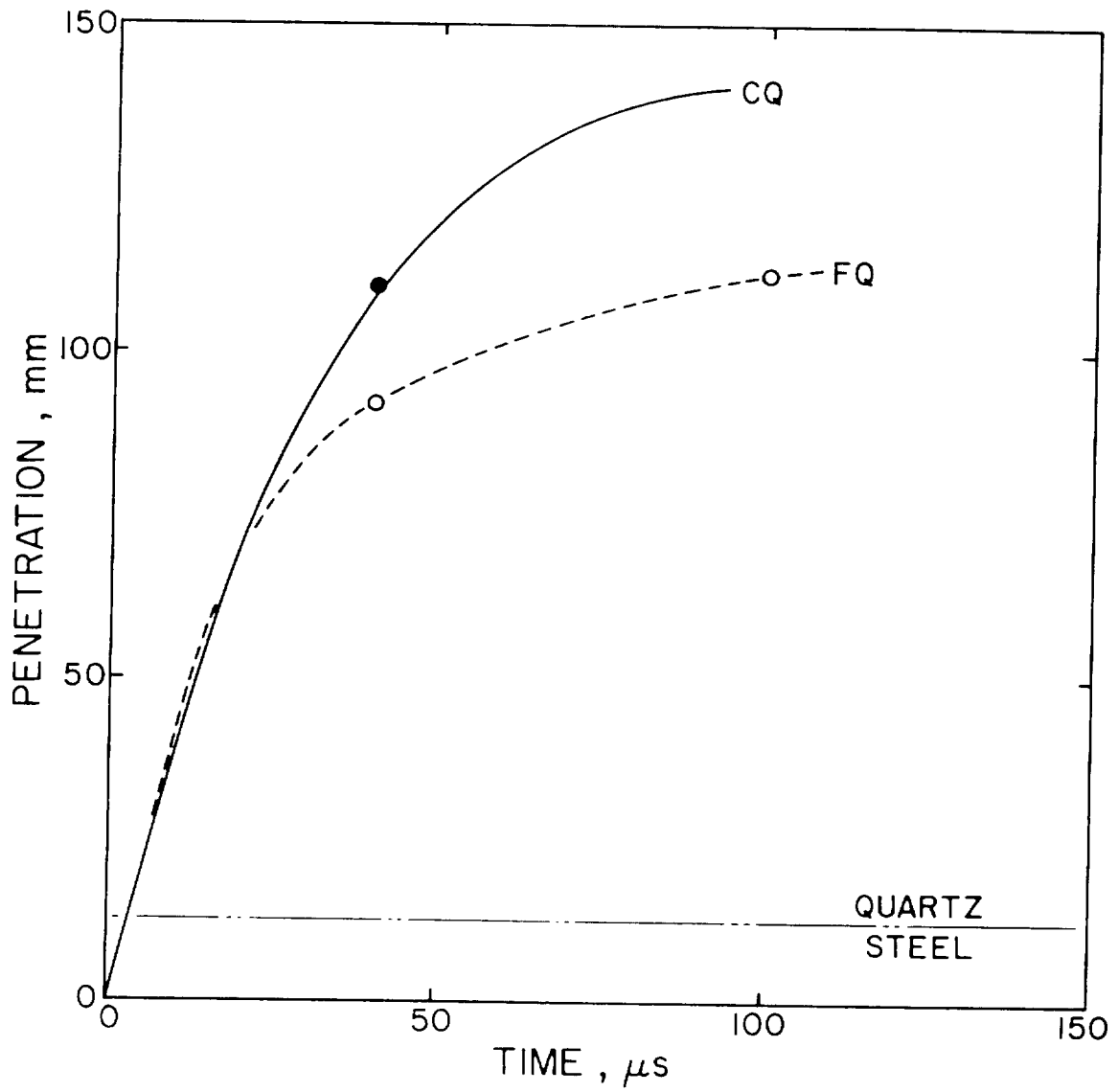Figure 9. Comparison of Penetration-Time Data for Jet Penetration Into Fused Quartz (FQ) and Crystalline Quartz (CQ).

without the ferric-ion impurity that commonly imparts a green color to thick window glass. The glass used by Pugh et al. was identified as commercial soda-lime. Photographic measurements of penetration-time were conducted with both types of soda-lime glass.

2.4.3 Jet Penetration Into Soda-Lime Glass. Most of the photographic studies with soda-lime glass were conducted with front lighting, and the basic configuration is shown in Figure 6. The standoff in most tests was approximately 140 mm, and in these tests the glass was penetrated by a particulated jet. Two tests were conducted with a shorter standoff of approximately 50 mm, and in these tests the jet was continuous throughout most of the photographic sequence. One test was conducted with the soda-lime glass without ferric-ion impurity. This test was of interest because the glass was monolithic and contained small bubbles. All other tests were conducted with commercial soda-lime plate which had a thickness of 25 mm. Tests with a continuous jet will be described first.

Figure 10 shows sequential photographs of a continuous jet penetrating 25 mm thick plates of soda-lime glass. Photographs were at 1 μs intervals and were taken with strong front lighting and weak back lighting. These photographs show the boundary of the penetration path, the permanently densified volume surrounding the penetration path, the trailing fracture, and the fracture initiated at a bonded interface between glass plates. The penetration path is observed to open and then partially close. Since closure occurs before the surrounding glass undergoes brittle failure, it is concluded that closure is primarily associated with recovery from high pressures near the penetration front. The boundary of the permanently densified volume, which is initially at the yield stress, displays slight necking as a result of elastic recovery. The boundary layer of the penetration path is the only part of the target that is recovered intact. Surrounding target material fails into particles which are dispersed by the blast, while material in the penetration path is highly mobile and escapes as the target fails. The heated boundary layer is sufficiently plastic to resist brittle failure and survives with recognizable features. This boundary layer was found to have a thickness of approximately 1 mm.

Figure 11 shows penetration-time data for the test pictured in Figure 10. All of the experimental data are in close agreement with a curve generated by the penetration model
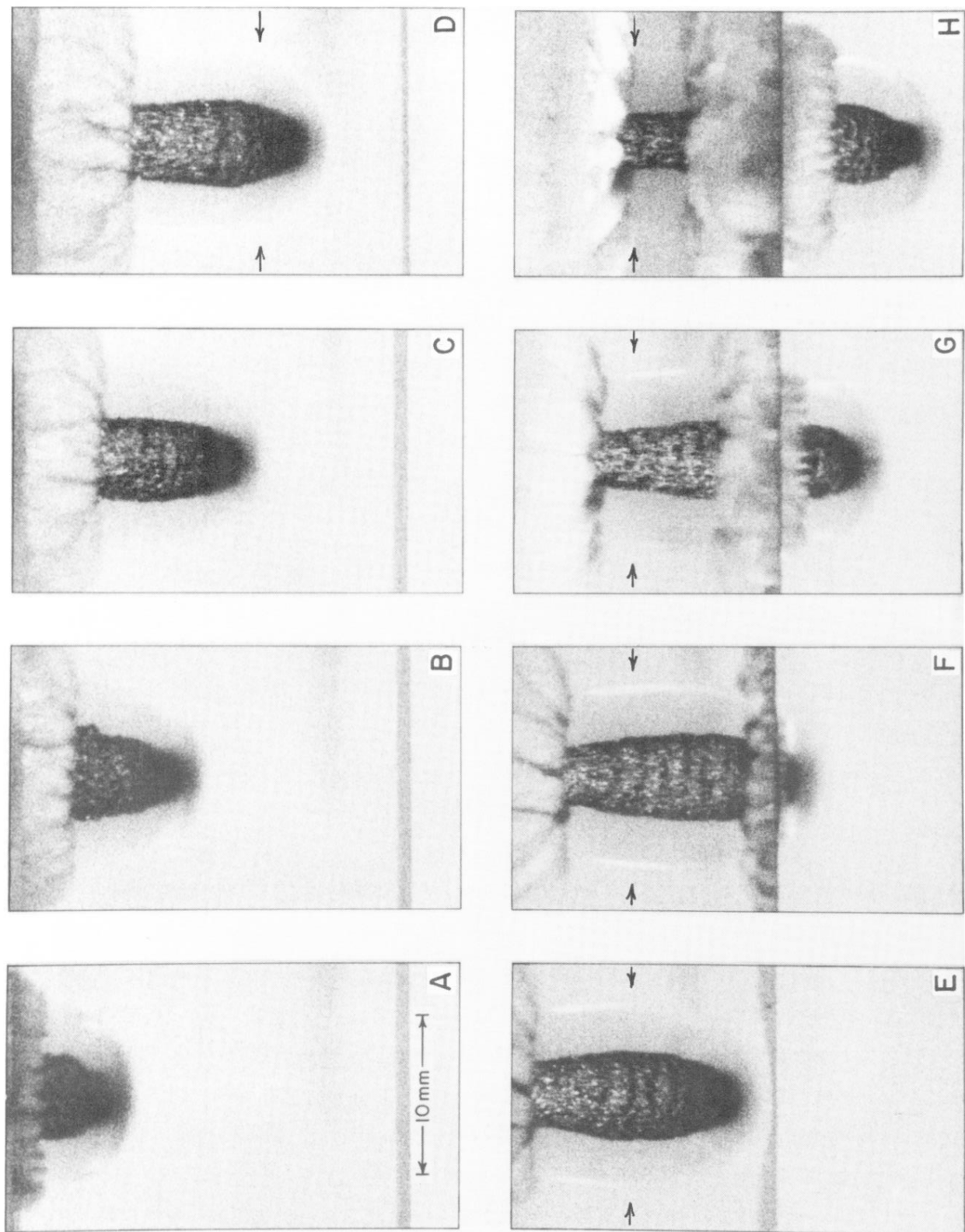
Figure 10. Photographs of a Soda-Lime Glass Target During Penetration by a Continuous Jet (Test 1).
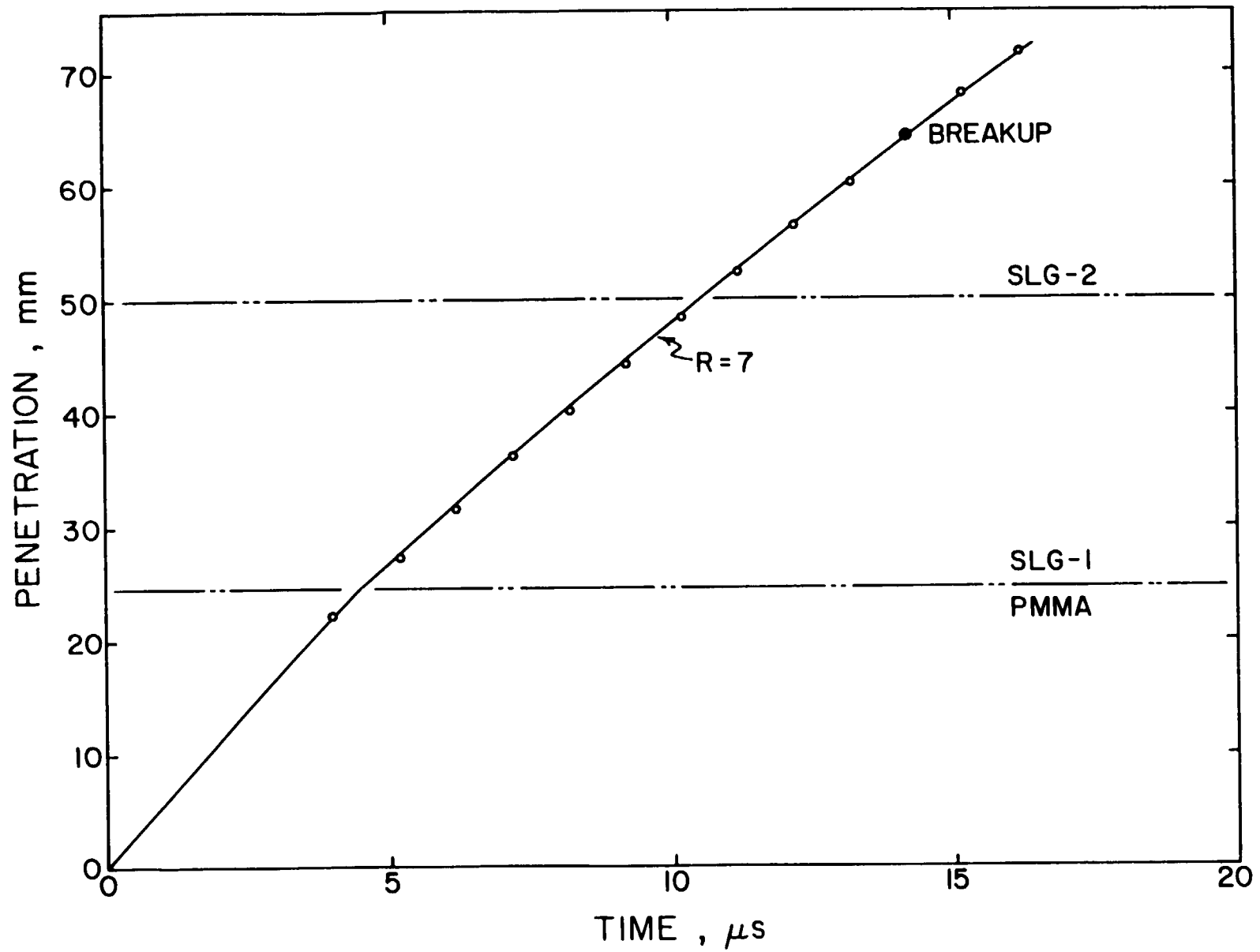
Figure 11. Penetration-Time Data for the Jet Penetration Shown in Figure 10.

with R = 7 GPa. There is no evidence of an increase in target resistance such as detected with fused quartz in Figure 7. Jet breakup, based on free-flight observations, is indicated on the penetration path and should have occurred at the end of the photographic sequence in Figure 10. Frame H in Figure 10 does show an irregularity at the end of the penetration path that resembles penetration by a jet particle. Later, similar features will be observed during penetration by a jet that is definitely particulated.

The target configuration in Figure 6 was modified for a second penetration test with a continuous jet. Thickness of the PMMA cover was reduced to 3.2 mm and a 25-mm thickness of steel was added at the front. A hole, 4.8 mm in diameter, was drilled through the steel to admit the jet. It was anticipated that the confinement provided by this steel plate would enhance path closure close to the PMMA-glass interface. Sequential photographs from this test are shown in Figure 12. When compared with the photographs in Figure 10, the penetration path in this test is highly asymmetrical, with protrusions and regions of intense self-luminosity that were not observed in the preceding test with a continuous jet. These features suggest a greater interaction between the jet and the glass target.

Figure 13 shows penetration-time data from the second test with a continuous jet. Data during the first 9 μs of penetration into glass were in agreement with a curve generated by assigning a target resistance of 7 GPa. However, the target resistance then increased abruptly and a value of 40 GPa was necessary to produce agreement with the final three data points. Jet breakup should have occurred after the final point.

Photographs from both tests with a continuous jet were measured to determine how the diameter of the penetration path, including the boundary layer, varied with time. Path diameters were measured at approximately the same location in each test, and the locations are indicated by arrows in Figures 10 and 12. In Figure 14, the path diameters are plotted as a function of time. In the first test, which had a highly symmetrical penetration path, the path opened to its maximum diameter in 2 μs and then partially closed before fracture obscured the measurement location. In the second test, the diameter began to deviate from the trend of the first test at 2–3 μs, and reopening was clearly established at 5 μs. It is assumed that this resulted from an interaction with elements of the jet behind the penetration front. In Figure 15, the penetration path from Figure 13 is replotted along with a path for the jet element that
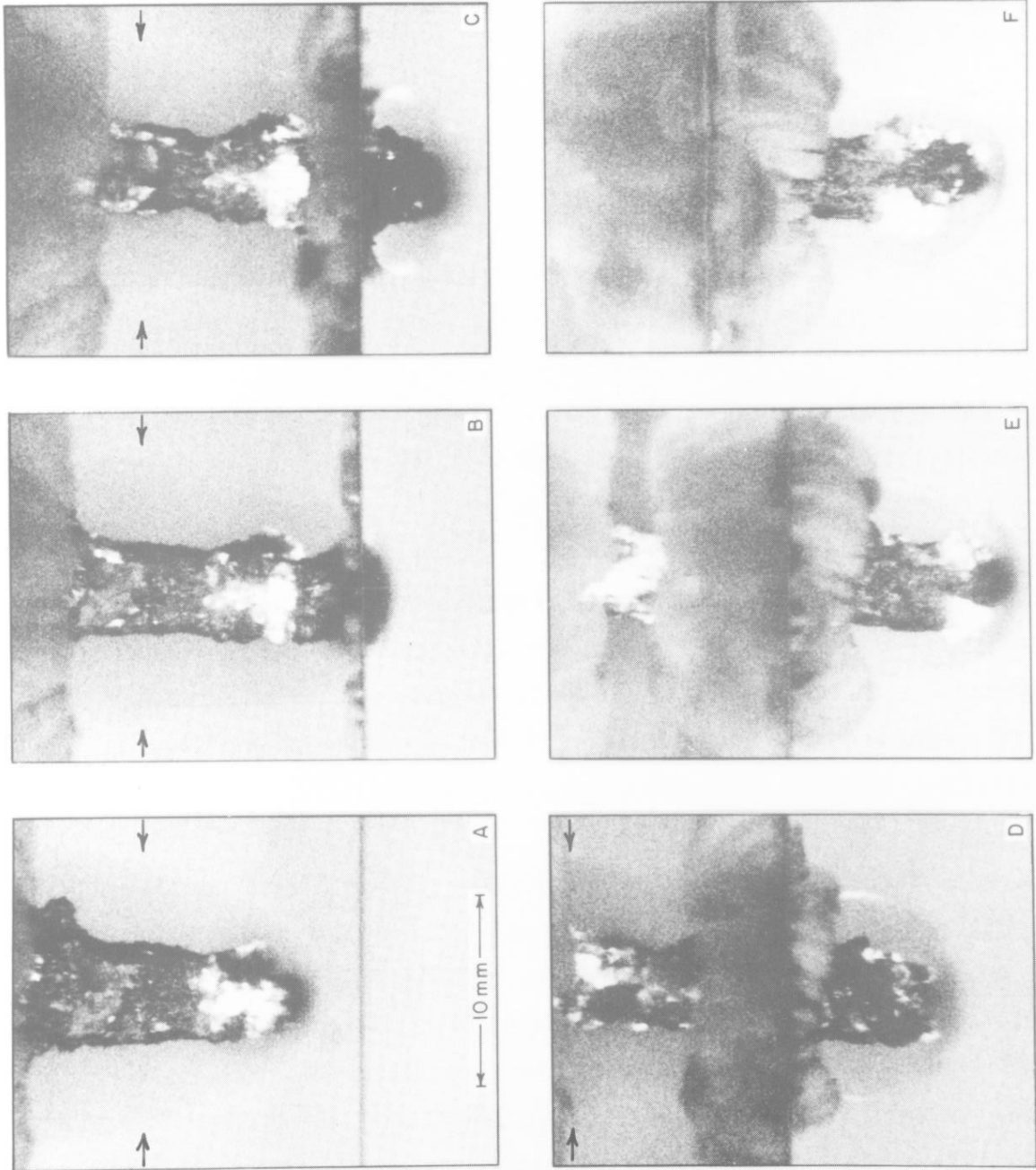
Figure 12. Photographs of a Soda-Lime Glass Target During Penetration by a Continuous Jet (Test 2).
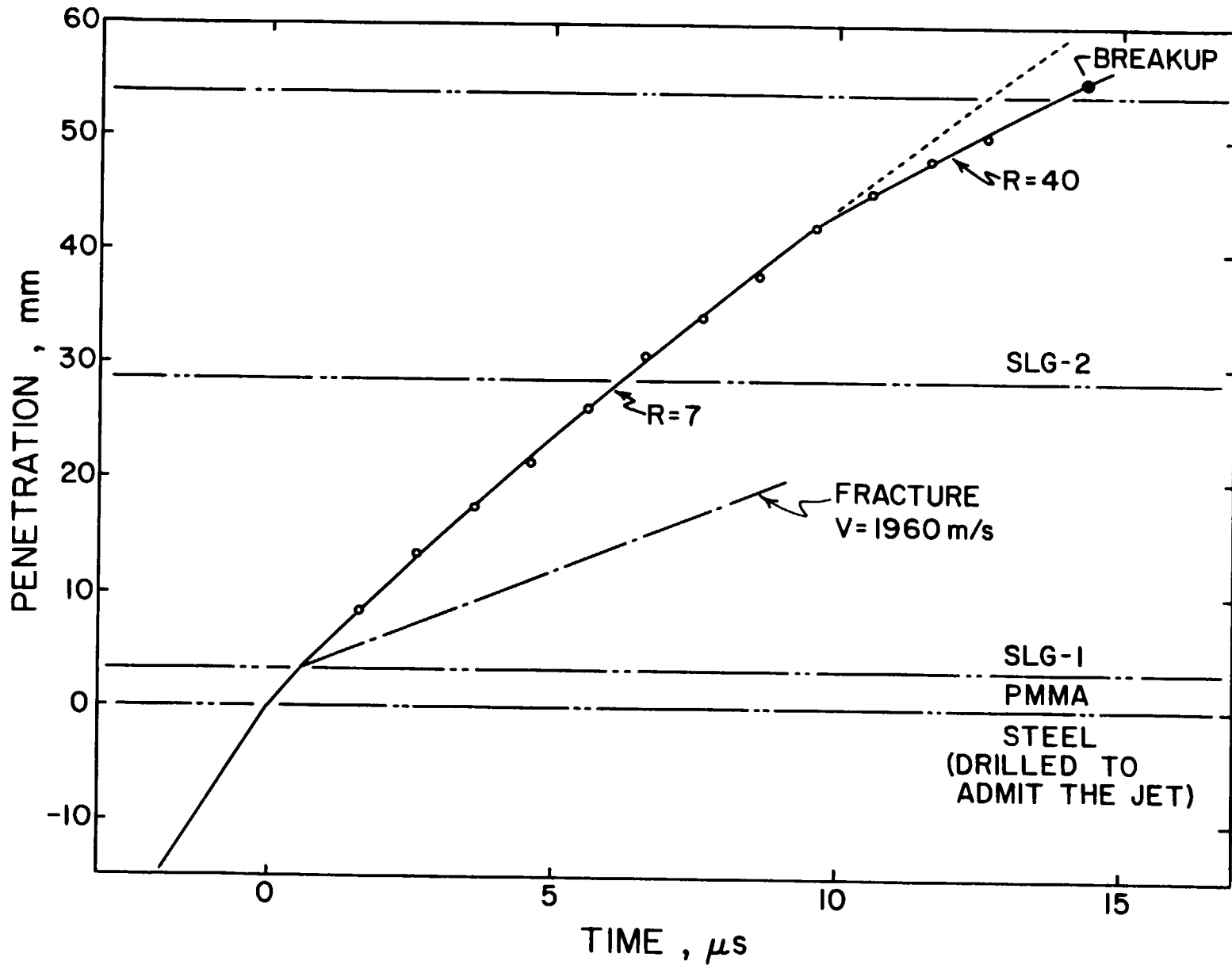
Figure 13. Penetration-Time Data for the Jet Penetration Shown in Figure 12.
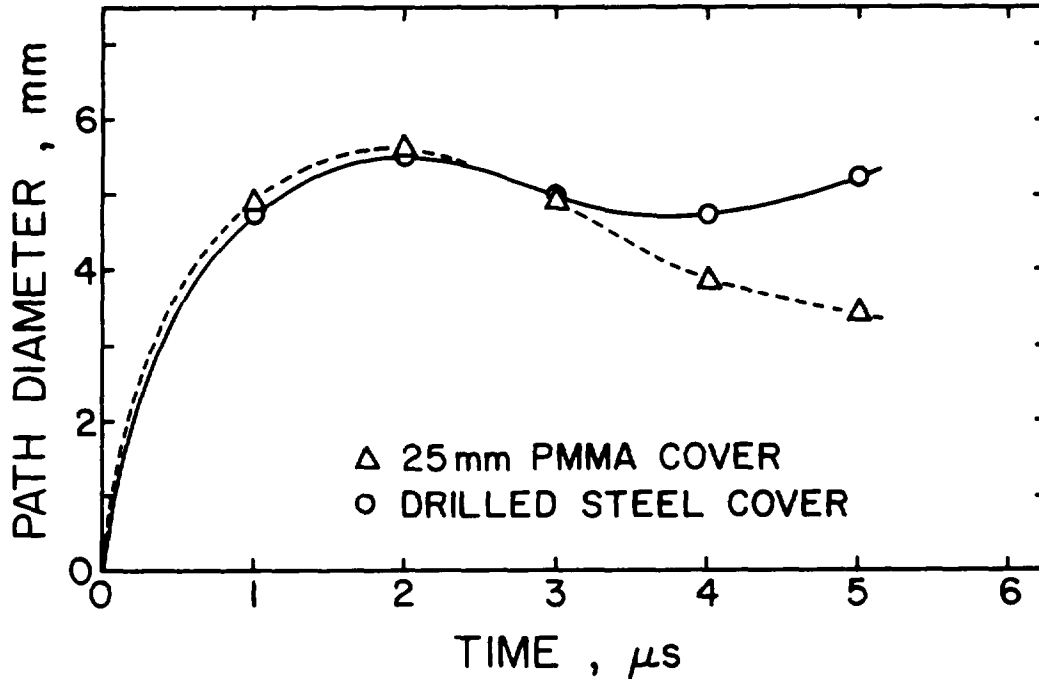
Figure 14. Path Diameter as a Function of Time (Continuous Jets).

arrives at the transition point where the target resistance increases. This jet element reached the location of diameter measurements approximately 2.3 μs after the tip. This time is in general agreement with the 2–3 μs time at which the curves begin to deviate in Figure 14.

Two factors probably contributed to features of the penetration path in Figure 14. First, the presence of a thick steel cover provided confinement which aided path closure close to the glass surface. Second, earlier studies (Zernow et al. 1975; Meyer 1987) showed that reflected debris particles can disrupt a jet as it passes through a tubular opening. The continuous jet in the second test was undoubtedly disrupted while passing through the 4.8-mm diameter hole drilled through the steel cover, and the disruptions caused early interactions between the jet and the closing penetration path. Protrusions and regions of intense luminosity in Figure 12 are evidence of such interactions.

Photographic tests were also conducted to determine how a particulated jet interacts with a target of soda-lime glass. Figure 16 shows a sequence of photographs taken at 1-μs

22
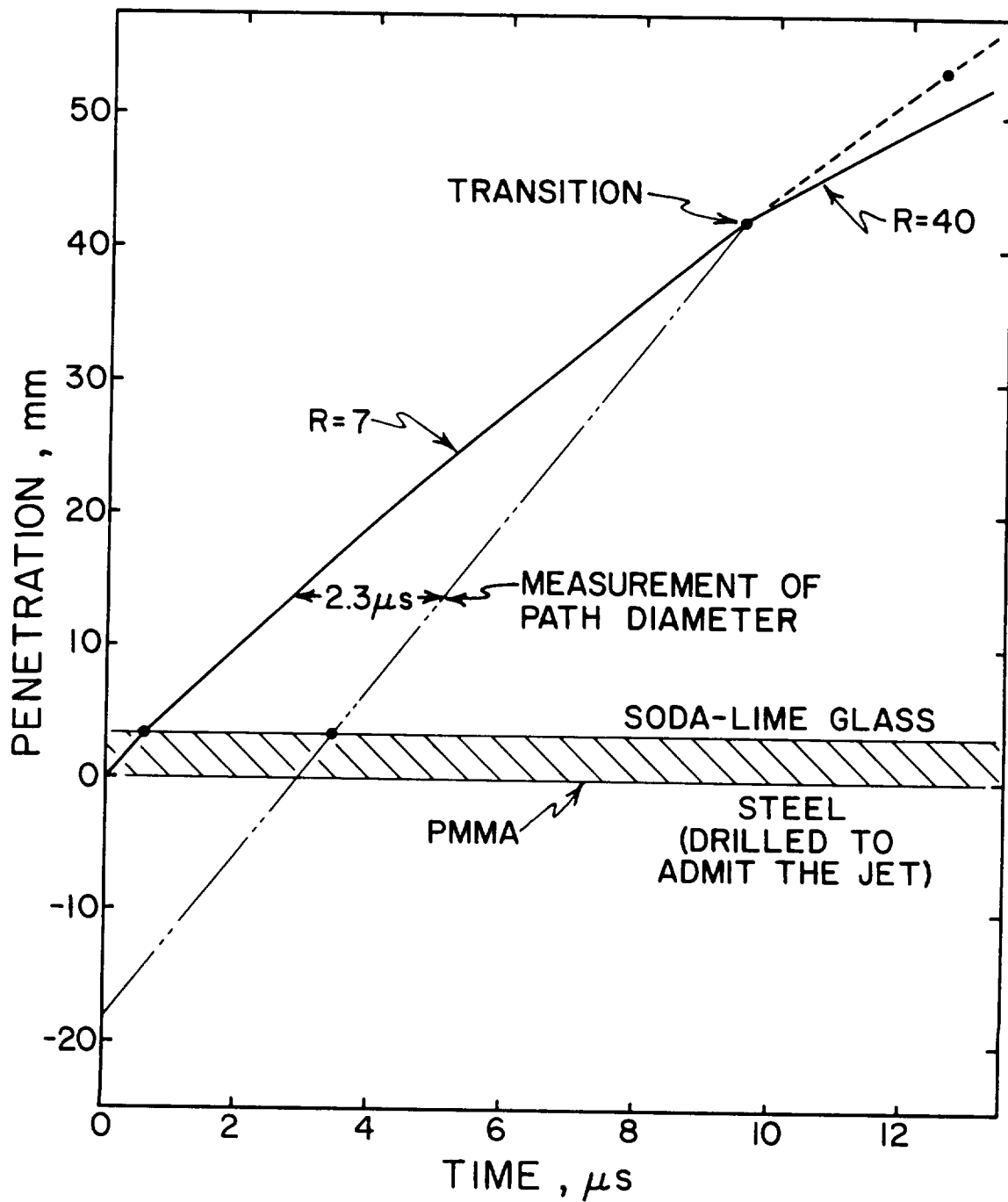
Figure 15. Penetration-Time Curves From Figure 13, Including a Path for the Jet Element That Arrives at the Transition Point.

23
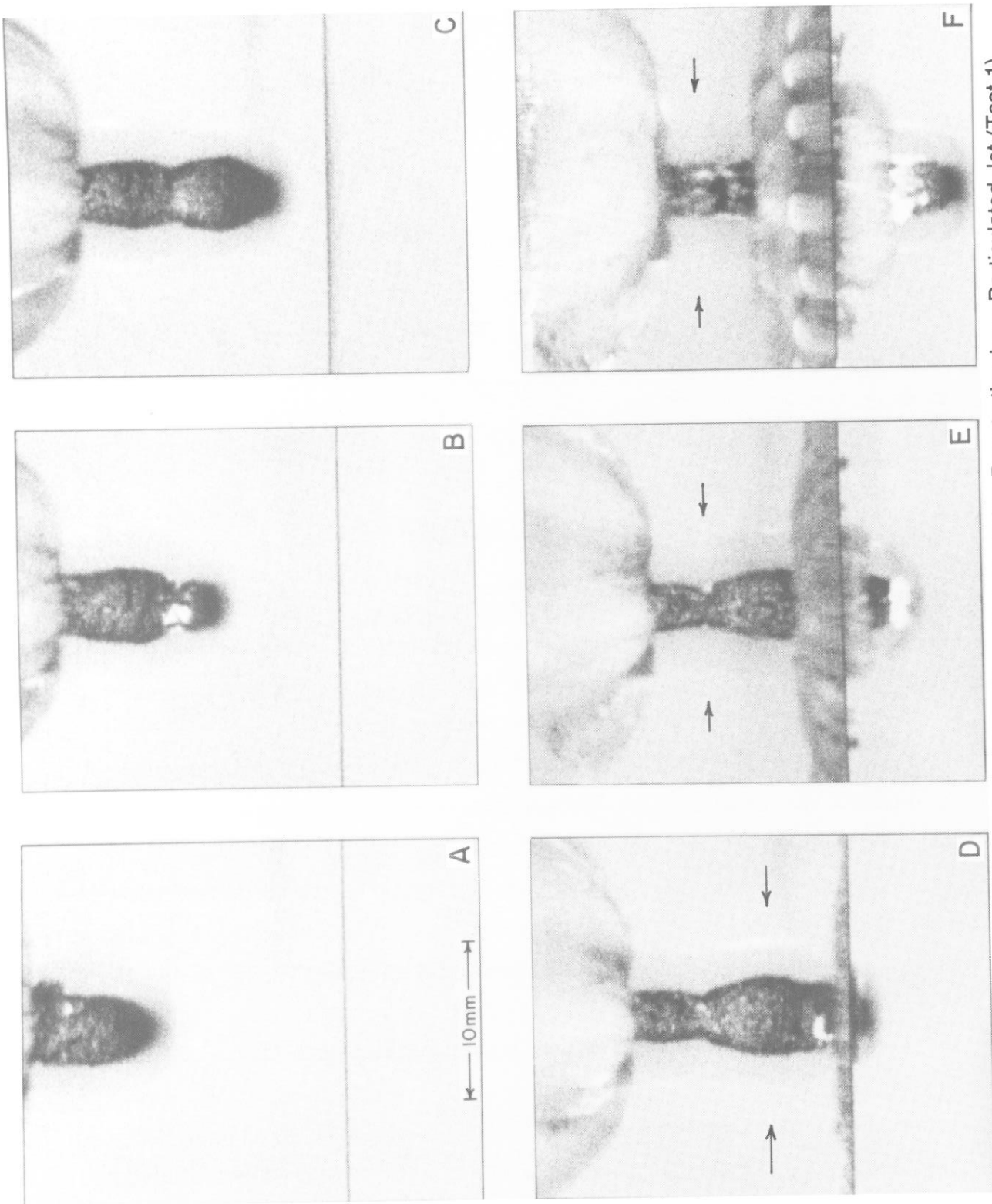
Figure 16. Photographs of a Soda-Lime Glass Target During Penetration by a Particulated Jet (Test 1).

24

intervals during penetration by a particulated jet. The basic features are similar to those observed with a continuous jet in Figure 10. Photographs show the boundary of the penetration path, the permanently densified volume surrounding the penetration path, the trailing fracture, and the fracture initiated at a bonded interface between glass plates. However, these photographs show an undulating penetration path which opens and partially closes with the impact of each successive jet particle. Intense self-luminosity is associated with each impact. Reopening of the penetration path after partial closure is evident at the neck region, which is indicated by arrows in Frames E and F. Path diameters were measured both at the neck region and at the maximum which is indicated by arrows in Frame D. Diameters at both locations are plotted against time in Figure 17. At the neck location, reopening of the penetration path begins approximately 3.3 μs after the initial opening. This reopening is attributed to the interaction with a jet particle as it passes the location of the measurement in Frame F.

Figure 18 shows penetration-time data for the test pictured in Figure 16. As in the case of a continuous jet, the initial part of penetration into soda-lime glass is described by the model using an assigned target resistance of 7 GPa. At 16.6 μs, the final datum point is displaced significantly below the extrapolated path for R = 7 GPa, providing minimal evidence of an increase in target resistance. The jet element arriving at the apparent transition point passes the neck location 3.1 μs after the penetration front, in close agreement with the reopening time in Figure 17. This agreement increases confidence in the final datum point of Figure 18. With the highly symmetrical penetration path in Figure 16, reopening at the neck region is clearly the first evidence of an interaction with jet elements behind the penetration front.

The penetration pictured in Figure 19 was obtained with a test configuration nearly identical to the one for the preceding test. However, this second test with a particulated jet used only front lighting. Without back lighting, the permanently densified region cannot be seen. In this test, the penetration path lacks the symmetry observed in the preceding test. There are numerous protrusions and regions of intense self-luminosity that indicate a strong interaction between the target and jet elements behind the penetration front. This different behavior is attributed to round-to-round variations of the shaped charge. The penetration-time data for this test are plotted in Figure 20. As in preceding tests with soda-lime glass, the first
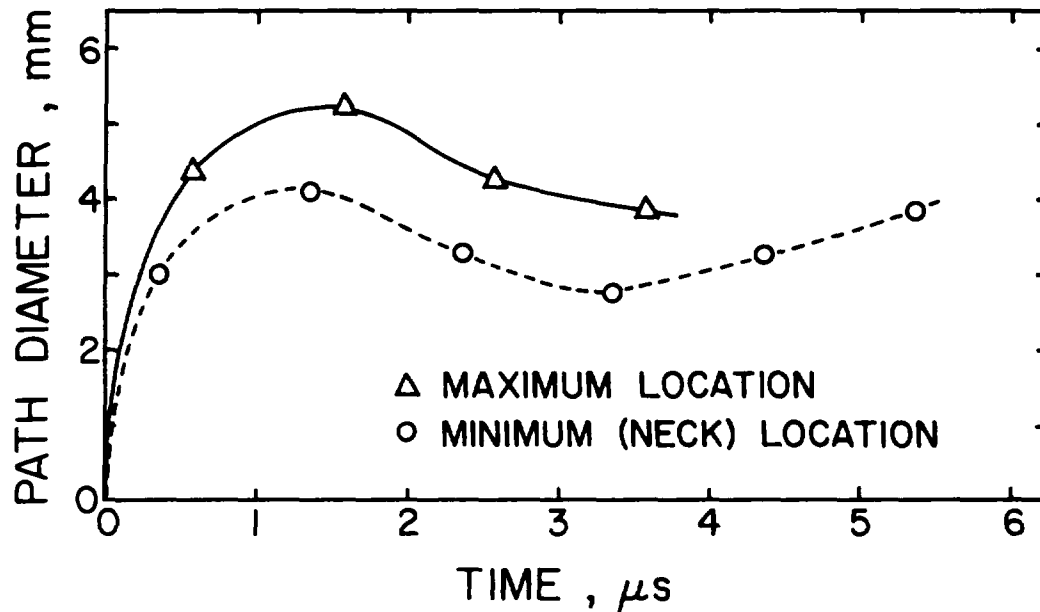
Figure 17. Path Diameter as a Function of Time (Particulated Jet).

part of penetration is described by the model using a target resistance of 7 GPa. However, after approximately 9 μs of penetration into the glass, there is a pronounced deviation, and later data can be described only by assigning a target resistance of 80 GPa. This large increase in resistance must follow directly from the strong photographic evidence of jet-target interactions behind the penetration front.

Photographs from a third test with a particulated jet are shown in Figure 21. Only back lighting was used for this test. Increases in the index of refraction within permanently densified glass, as shown by measurements of Arndt, Hornemann, and Muller (1971), cause strong refraction of the back light and obscure detail behind the penetration front. Without multiple shock waves, visible in the original photographs, it would not be obvious that penetration was by a particulated jet. Refraction also obscures features of the penetration path that provide evidence of target interactions with jet elements behind the penetration front. However, the penetration-time data from this test, shown in Figure 22, clearly indicate that such interactions must have occurred. The initial part of penetration into soda-lime glass is again described by the model with R = 7 GPa. However, the point at 13.7 μs (9.3 μs into the
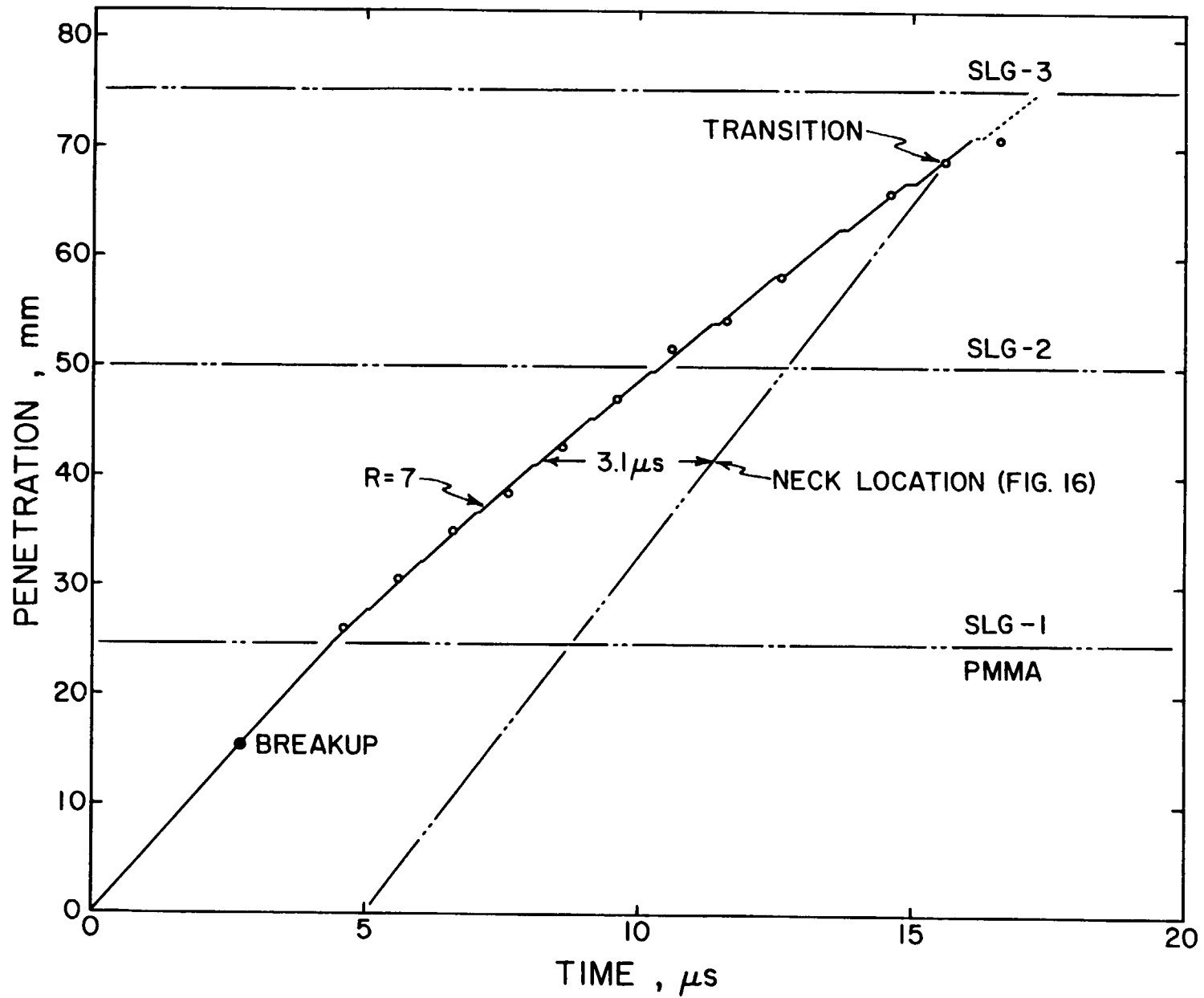
Figure 18. Penetration-Time Data for the Jet Penetration Shown in Figure 16.

27
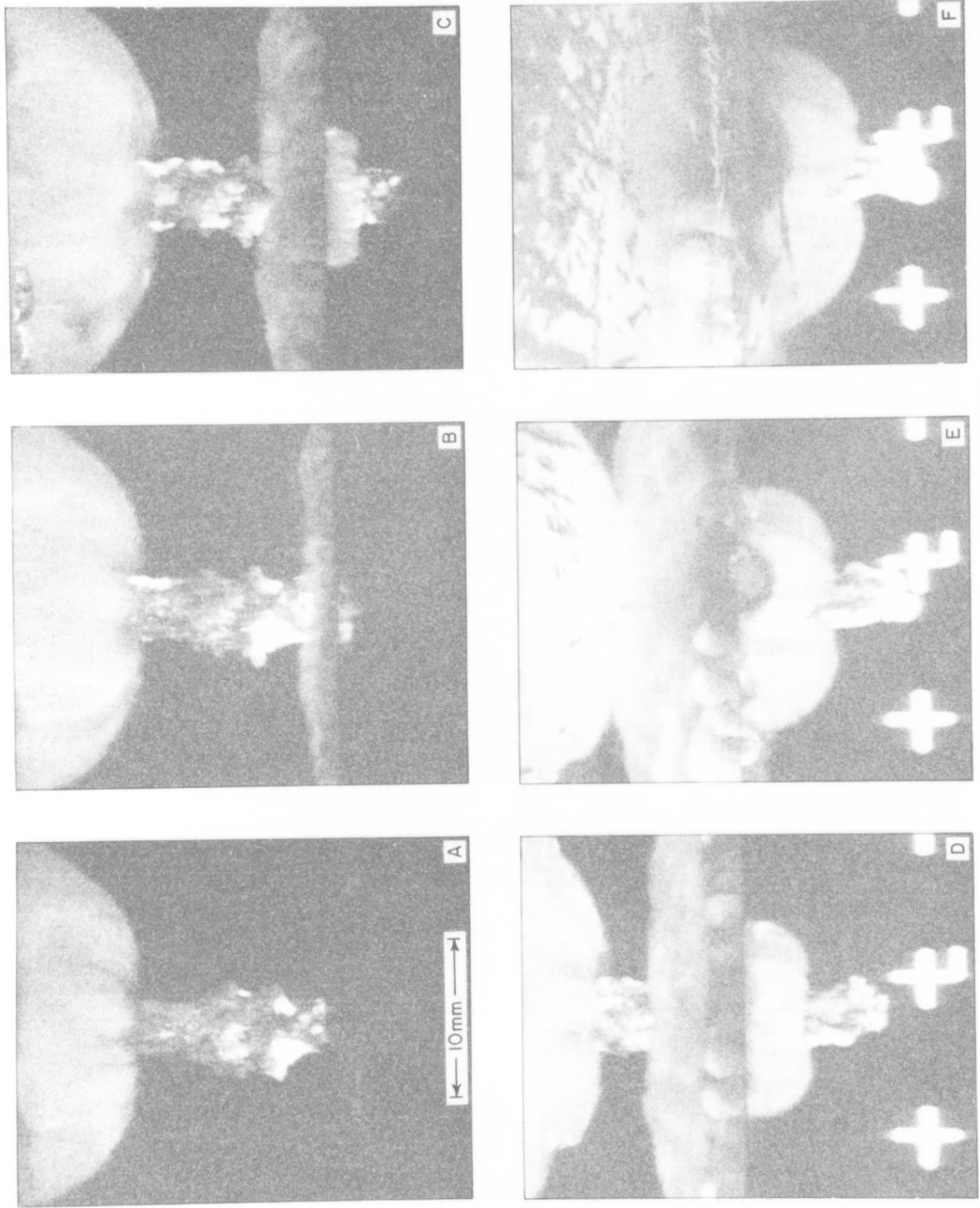
Figure 19. Photographs of a Soda-Lime Glass Target During Penetration by a Particulated Jet (Test 2).
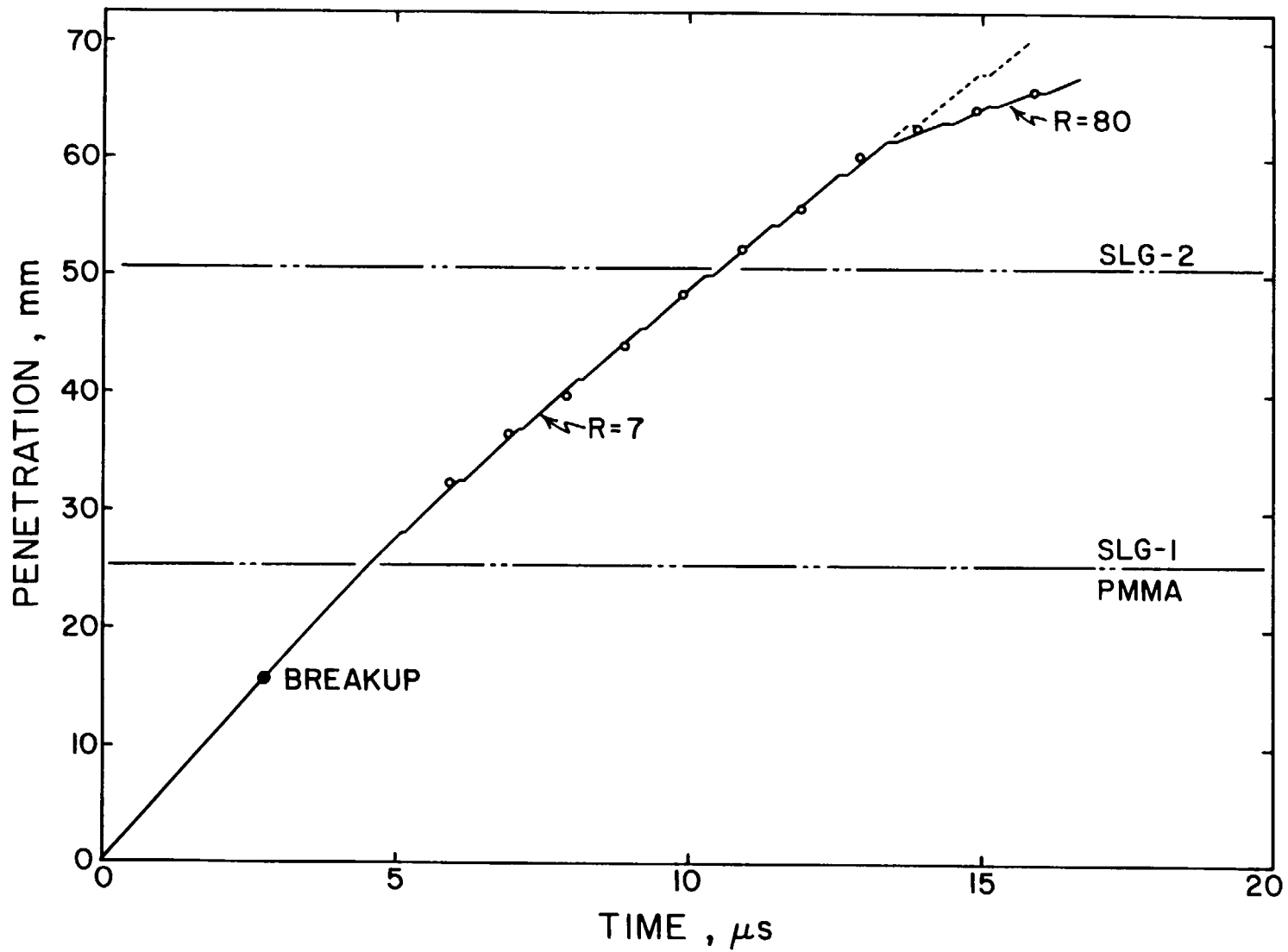
Figure 20. Penetration-Time Data for the Jet Penetration Shown in Figure 19.
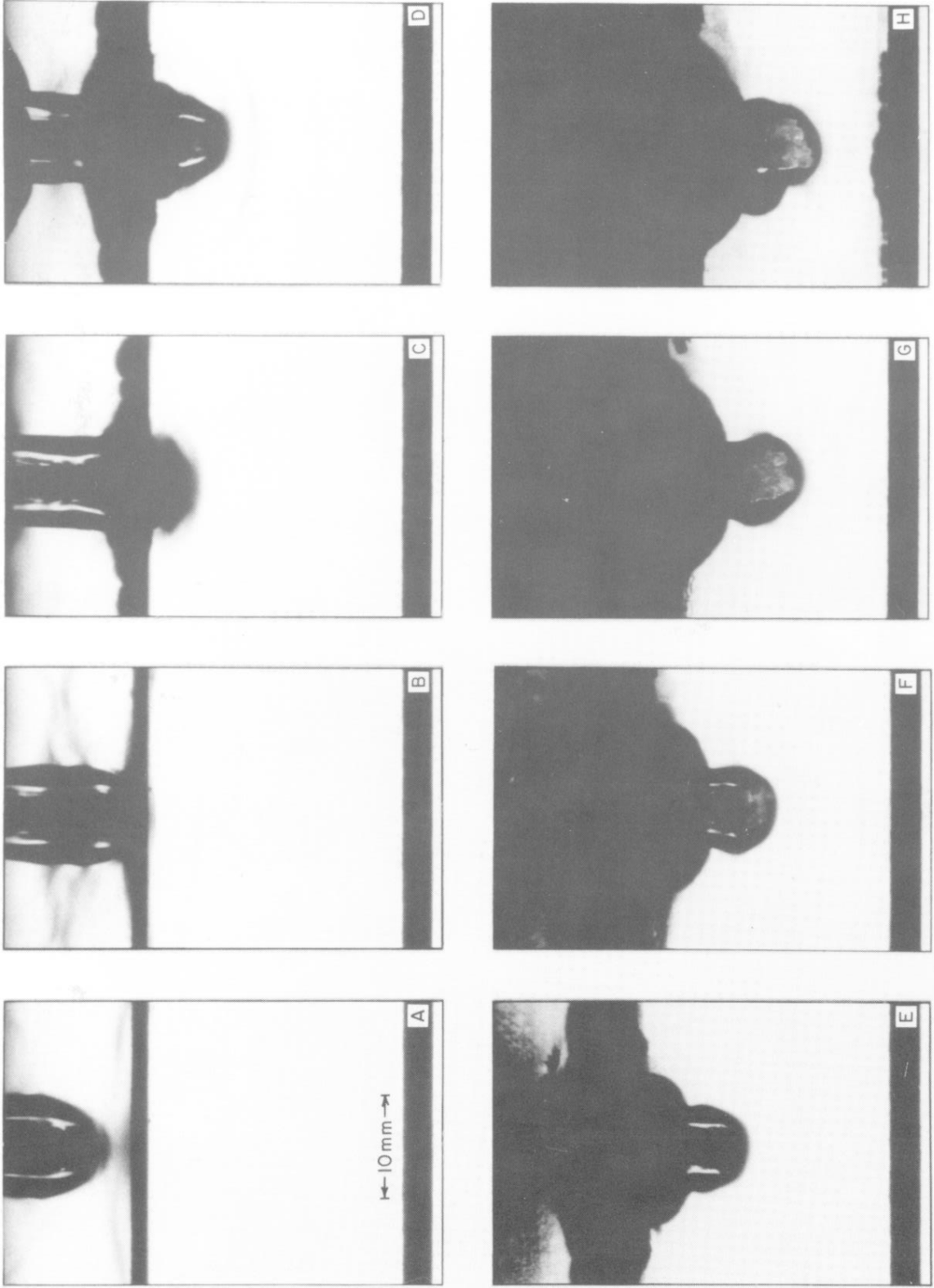
Figure 21. Back-Lighted Photographs of a Soda-Lime Glass Target During Penetration by a Particulated Jet (Test 3).
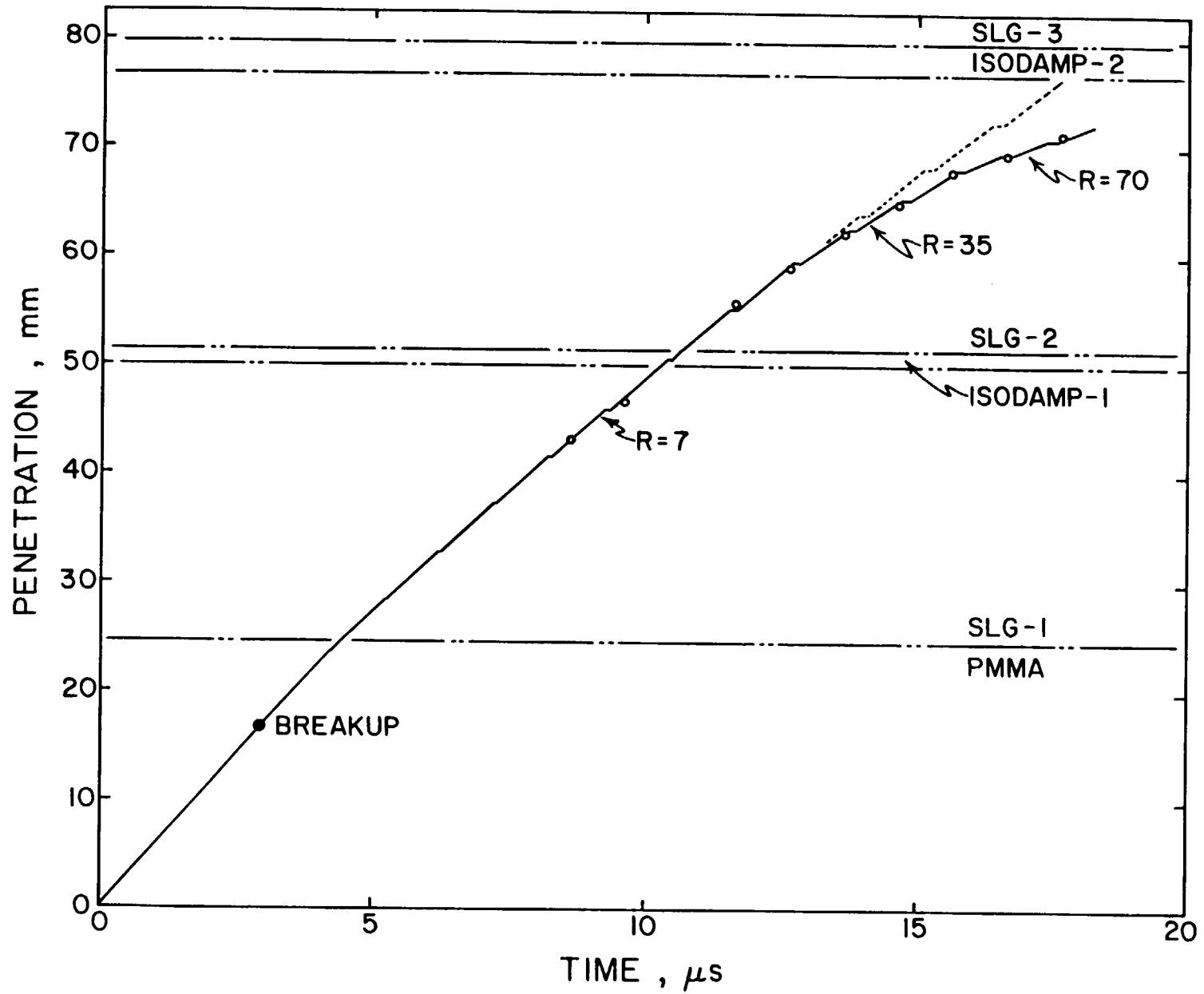
Figure 22. Penetration-Time Data for the Jet Penetration Shown in Figure 21.

glass) has deviated from the initial path, and over the next 4 μs the target resistance increases to 70 GPa. The presence of Isodamp between the glass plates in this test did not obviously influence the resistance to penetration, but it apparently delayed interface failure to provide an additional 2 μs for observations.

Monolithic soda-lime glass, without ferric-ion impurity, was used for the last photographic test to be reported. Consecutive frames from this fourth test with a particulated jet are shown in Figure 23. Strong interactions are indicated by the extremely irregular profile of the penetration path, and irregularities tend to mask the particle nature of penetration. Periodic emissions of light are the strongest evidence of particle impacts. Although this glass was monolithic and offered no interfaces where fracture could be initiated, it did contain many small bubbles which served as failure sites. Failure was not initiated by the impact shock, but instead it was observed to occur when a bubble encountered the boundary of permanently densified glass. Failure at bubbles occurs in Frame C, forward of the penetration path, and in Frames D–F, where failure sites developed at both the left and right of the penetration path.

Penetration-time data for the test with monolithic soda-lime glass are shown in Figure 24. The initial part of penetration into the glass is described by the model with R = 8 GPa. This value is higher than the initial resistance in soda-lime plate used in other tests. The velocity of trailing fracture was also higher (2,260 m/s, compared to 1,960 m/s for soda-lime plate). In this test, the target resistance deviated to higher values after only 6 μs of penetration into the glass. However, the higher values of target resistance were consistent with values determined in tests with soda-lime plate. Failure at bubble sites may have altered the closure rate in this monolithic glass, causing an early interaction with jet elements behind the penetration front. Resistance values in other tests with fused quartz and soda-lime plate never increased earlier than 9 μs after the onset of penetration into the glass. Based on this consistency, it is unlikely that a time as short as 6 μs would have resulted from round-to-round variation of the shaped charge.

2.5 Examination of Recovered Glass Targets. Radiographic targets that contained fused quartz were recovered and examined. Qualitative visual examinations could not readily distinguish these targets from recovered targets that contained borosilicate or soda-lime glasses. Figure 25 shows a fused quartz target that was sectioned to expose the entire

Figure 23. Photographs of a Monolithic Soda-Lime Glass Target During Penetration by a Particulated Jet (Test 4).

33

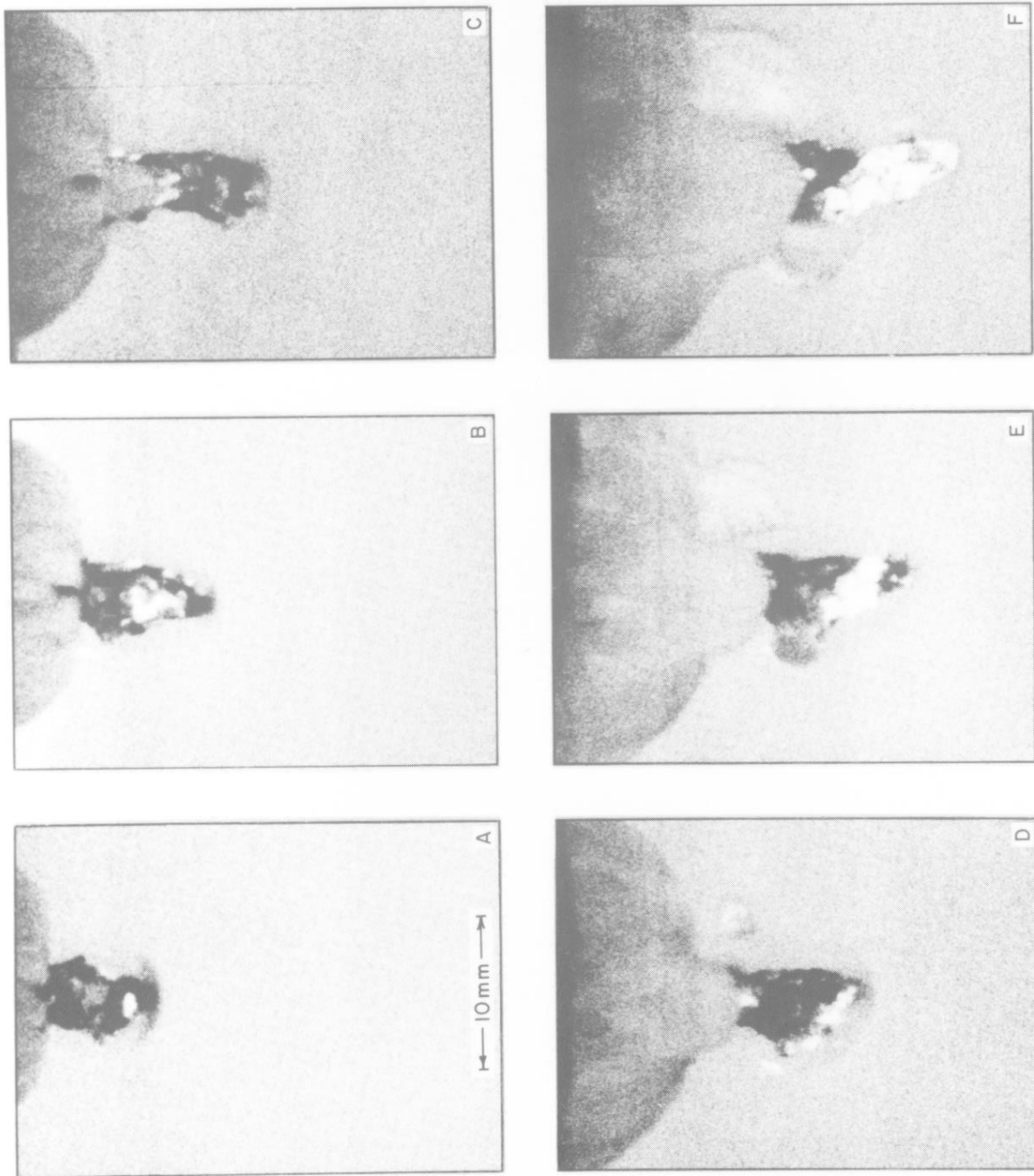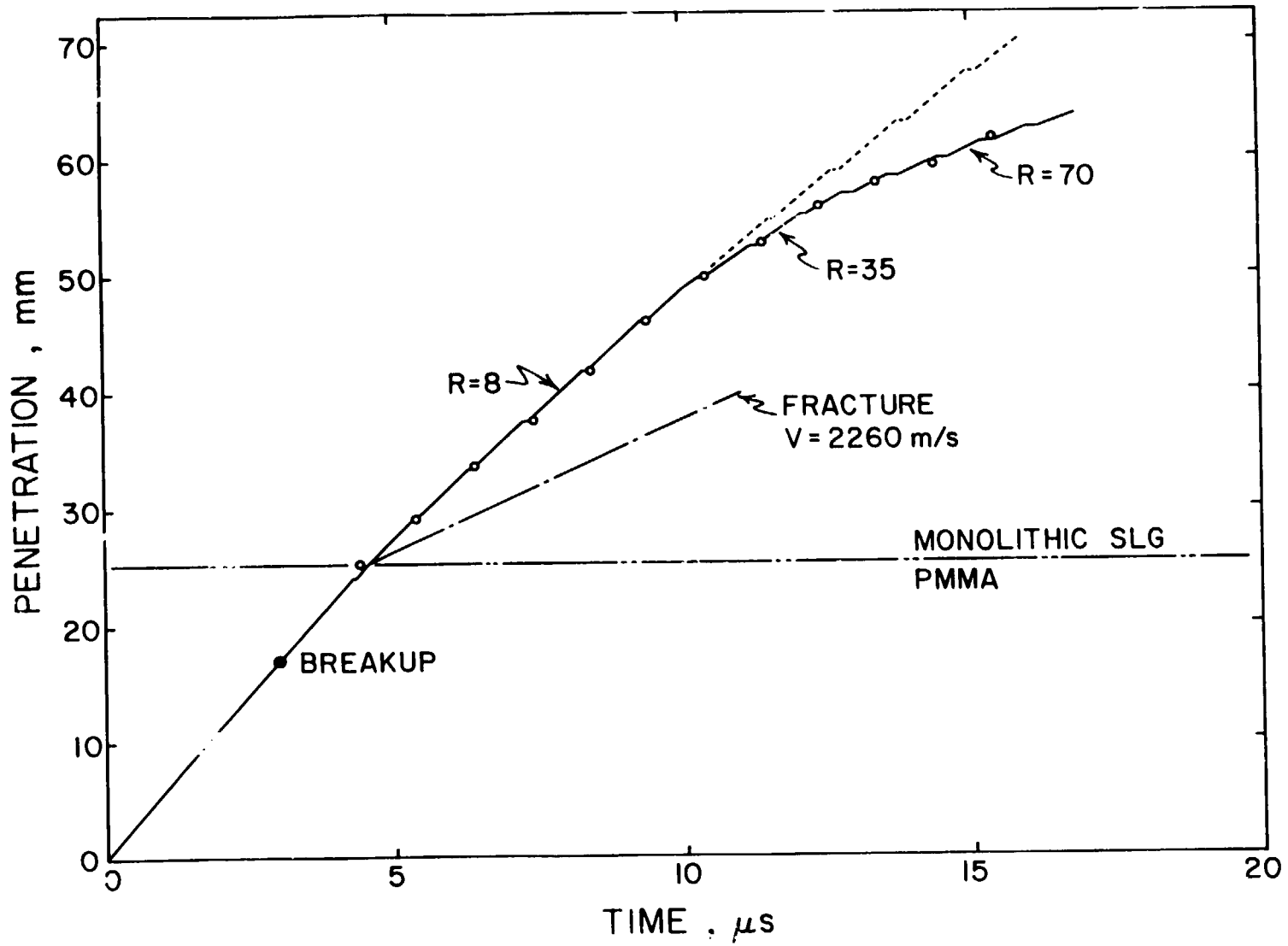Figure 24. Penetration-Time Data for the Jet Penetration Shown in Figure 23.

34
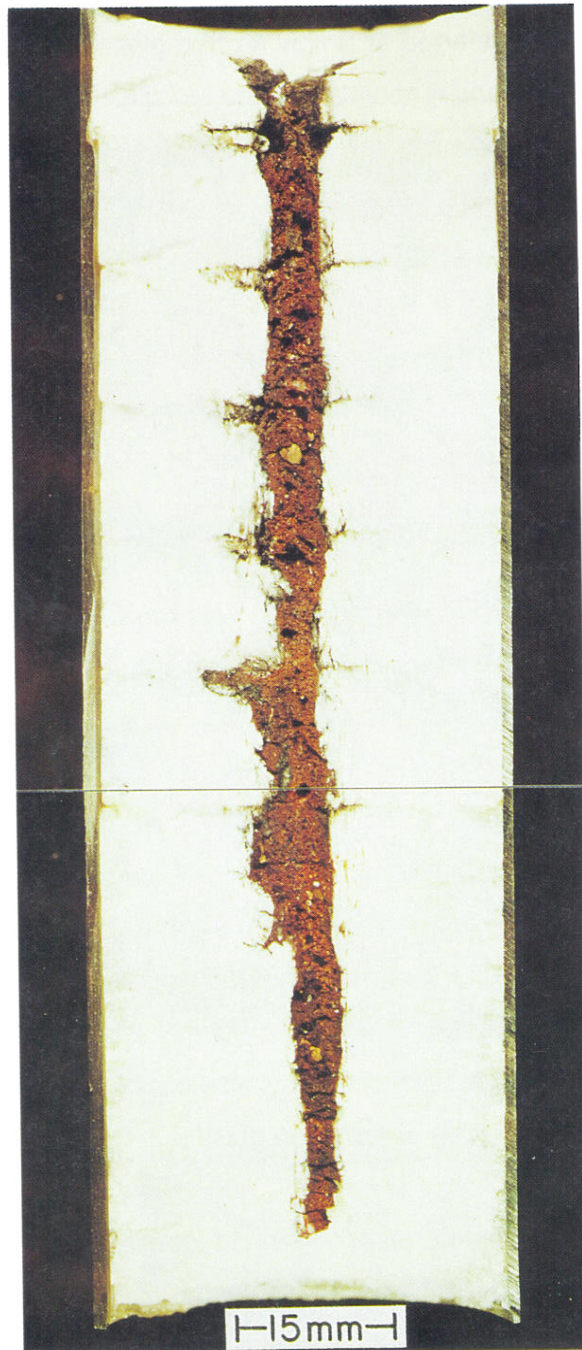
Figure 25. <u>Fused Quartz Target Sectioned to Expose the Penetration Path Filled With Red Glass</u>.

35

penetration path. The path is completely filled with a porous, opaque, red copper-glass. In the future, this material will be referred to simply as "red glass." A static x-ray of a recovered target is shown in Figure 26A, and it reveals that the red glass contains suspended copper spheres with diameters up to approximately 2 mm. An SEM micrograph of the red glass is shown in Figure 26B. The large copper sphere at the left in the micrograph has a diameter of 80 μm, while the smallest spheres approach a diameter of 1 μm. When a sample of red glass was examined at the Battelle Pacific Northwest Laboratories, it was concluded that the glass contained approximately 5% reacted/dissolved copper in addition to suspended copper spheres. Battelle cited a book by Weyl (1951) and noted the similarity to hematinone, which is an opaque red glass (glaze) containing suspended copper particles in the submicron range.

Red glass in the penetration path is very fluid just after it is formed and it frequently flows out of the target. Figure 27 shows red glass which was recovered after it flowed from the back of a fused quartz target that was perforated by the jet. Although a target may not be perforated, much of the red glass can also be forced out through the entrance hole if the slug is allowed to enter. This behavior in a borosilicate glass target is shown in Figure 28. Figures 28A and 28B show the void produced when the slug displaced red glass from the penetration path; Figure 28C shows part of the displaced red glass in a trap at the front of the target; and, Figure 28D shows slug material and red glass near the end of penetration. Radial cracks in Figure 28D are typical of failure near the end of penetration in targets of both glass and crystalline quartz. In Figure 28A, it may be noted that temperatures in the penetration path were high enough to remelt a significant thickness of pulverized glass around the penetration path (M identifies an area of remelted glass).

The porosity of red glass in the penetration path is tentatively attributed to localized heating that produces partial vaporization of the jet metal. Cavities in the red glass are commonly coated with small copper spheres and it is hypothesized that this deposit resulted from the condensation of copper vapor that initially filled the cavity. It was also observed that little porosity is produced when glass is penetrated by a steel jet, which should vaporize at a higher temperature. Penetration paths produced in glass by copper and steel jets are shown in Figures 29A and 29B, respectively. One glass target penetrated by an aluminum jet was examined, but the result was ambiguous. As shown in Figures 29C and 29D, material was ejected from the penetration path and deposited on an overhead plate. Vaporization of the

36

HIOmmH

A

B
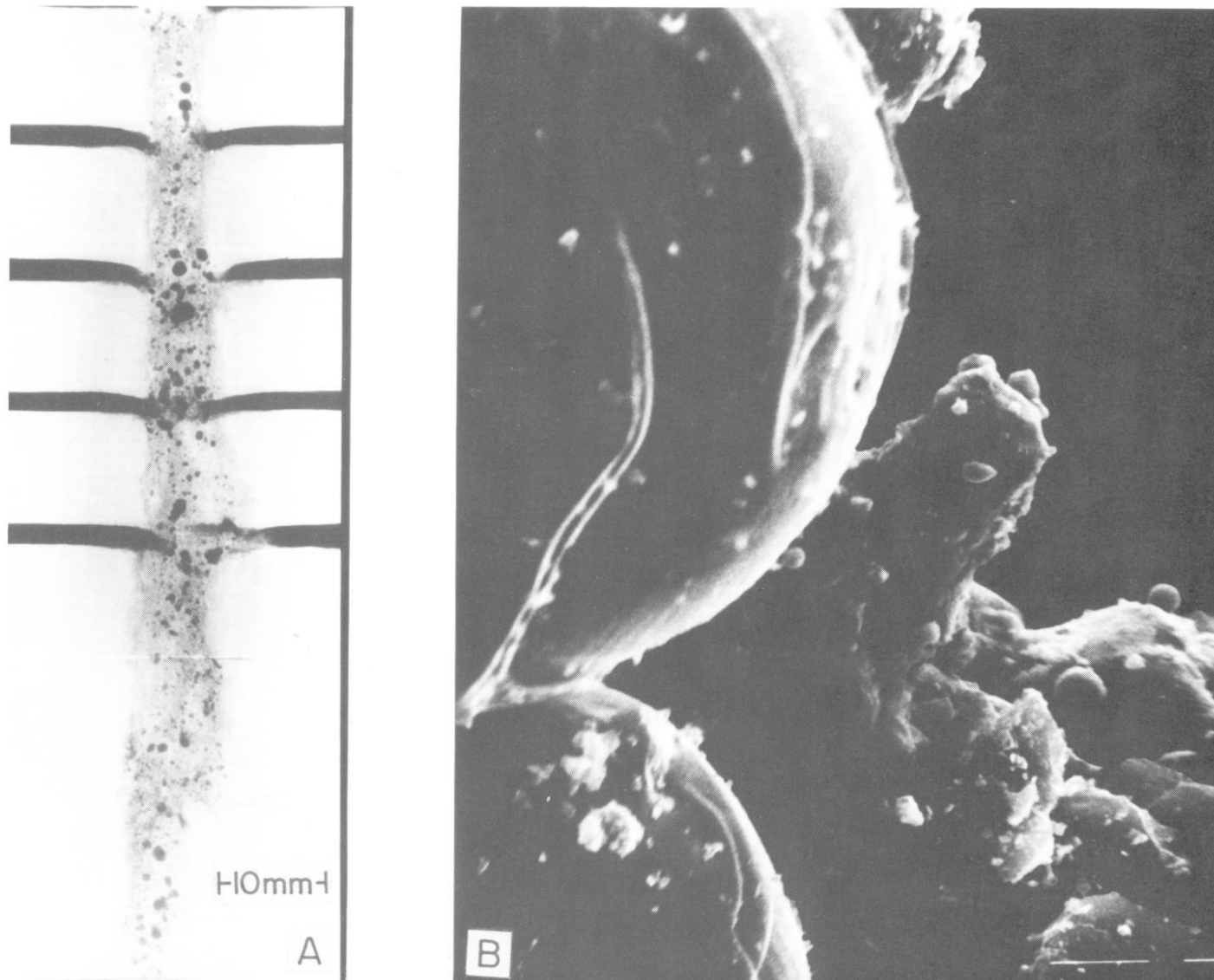
Figure 26. (A) Static Radiograph of the Penetration Path in Fused Quartz; (B) SEM Micrograph of Red Glass From the Penetration Path in Fused Quartz.
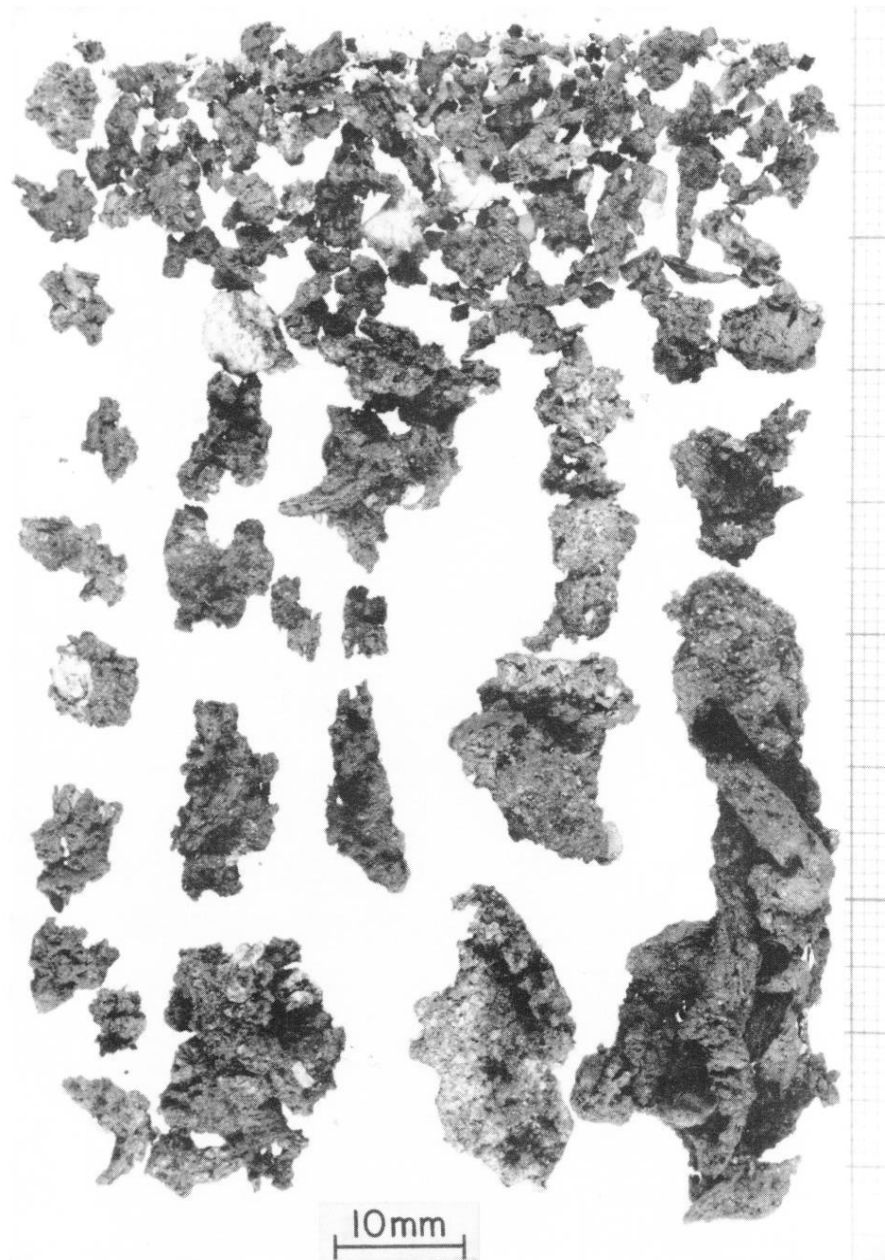
Figure 27. Red Glass That Flowed From the Back of a Perforated Fused Quartz Target.
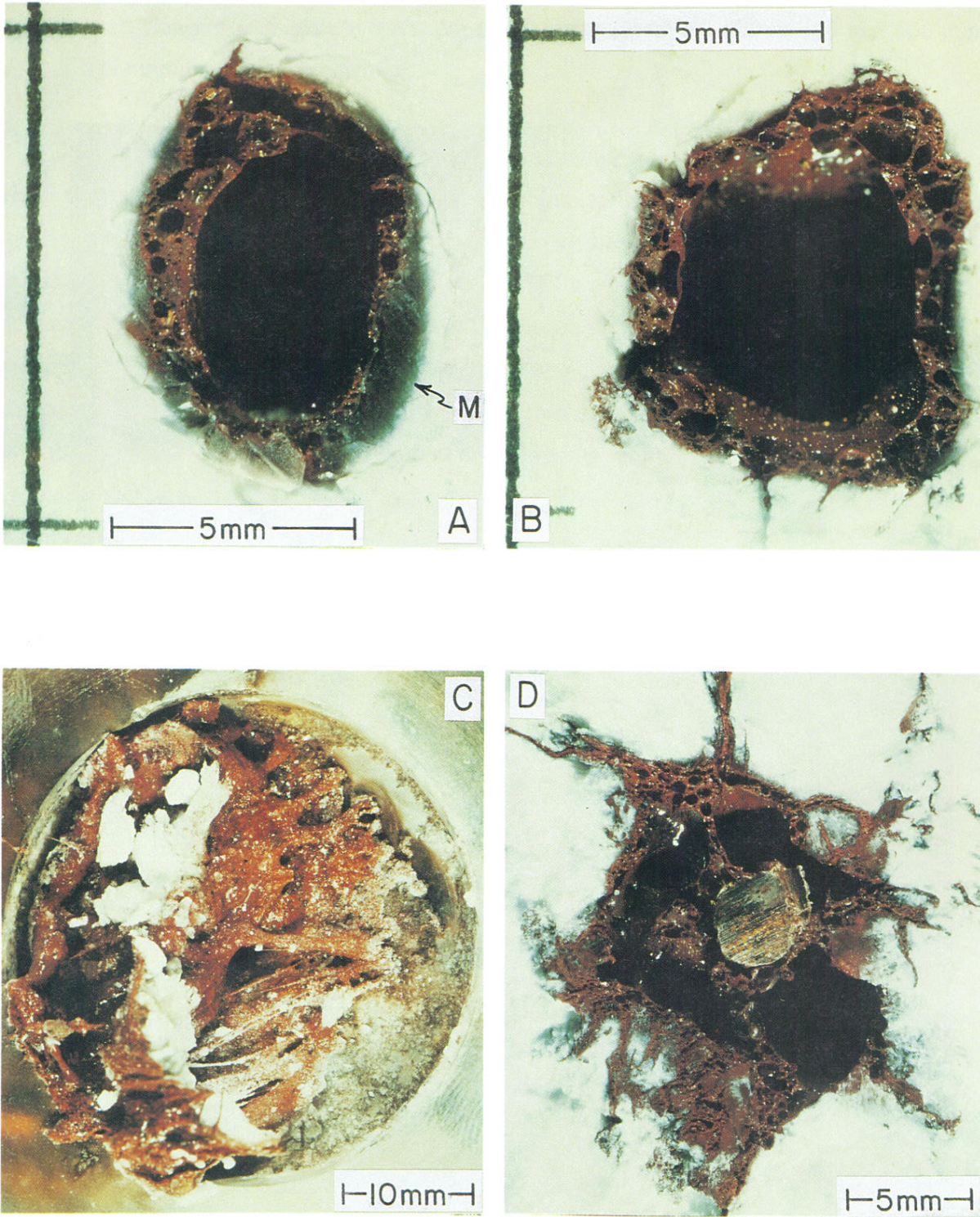
Figure 28. Recovered Target of Borosilicate Glass Showing Red Glass Displaced When the Slug Entered the Target.
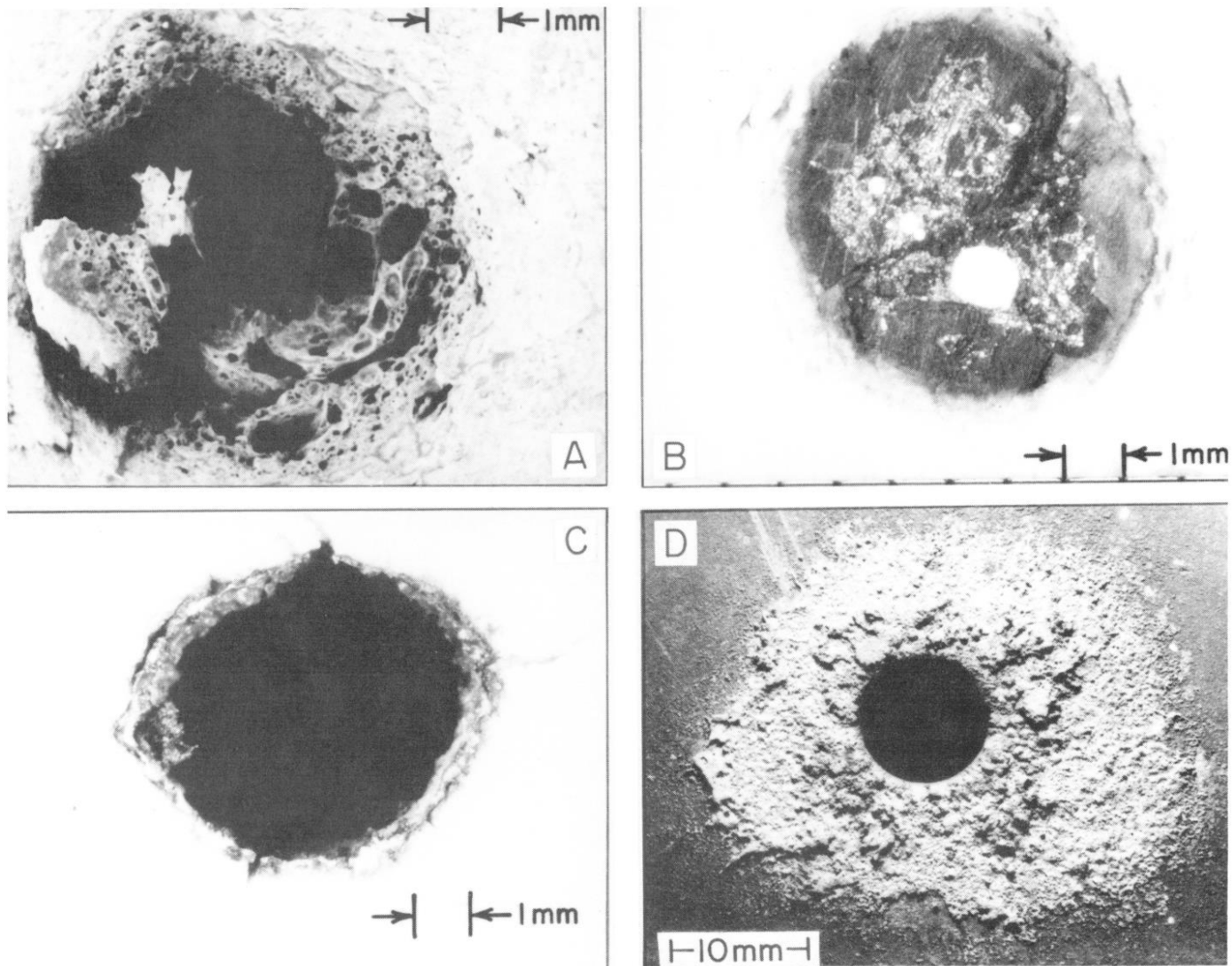
Figure 29. Glass Targets Penetrated by (A) a Copper Jet, (B) a Steel Jet, and (C) an Aluminum Jet; (D) is a Deposit of Material Ejected From the Penetration Path in (C).

aluminum jet could have contributed to the ejection, but the penetration model indicated that aluminum erosion products should travel out of the target at velocities from 700 to 2,500 m/s without a contribution from vaporization.

Evidence indicates that there is a significant interaction between the jet and red glass which fills the penetration path. Figure 26A, for example, shows a great amount of jet material suspended as spheres in the red glass. Additional evidence is provided by Figure 30, which shows a section of the penetration path produced in fused quartz by a small and relatively slow copper jet. In this test, red glass flowed into spaces between jet particles, with the exception of a channel that persisted between the two large central particles. These two particles are tapered, which gives evidence of erosion as they penetrated the red glass. Interaction with the red glass was strong enough to arrest the forward motion of the entire sequence of jet particles. The high melt viscosity of fused quartz was probably a factor in the resistance to particle penetration in this test.
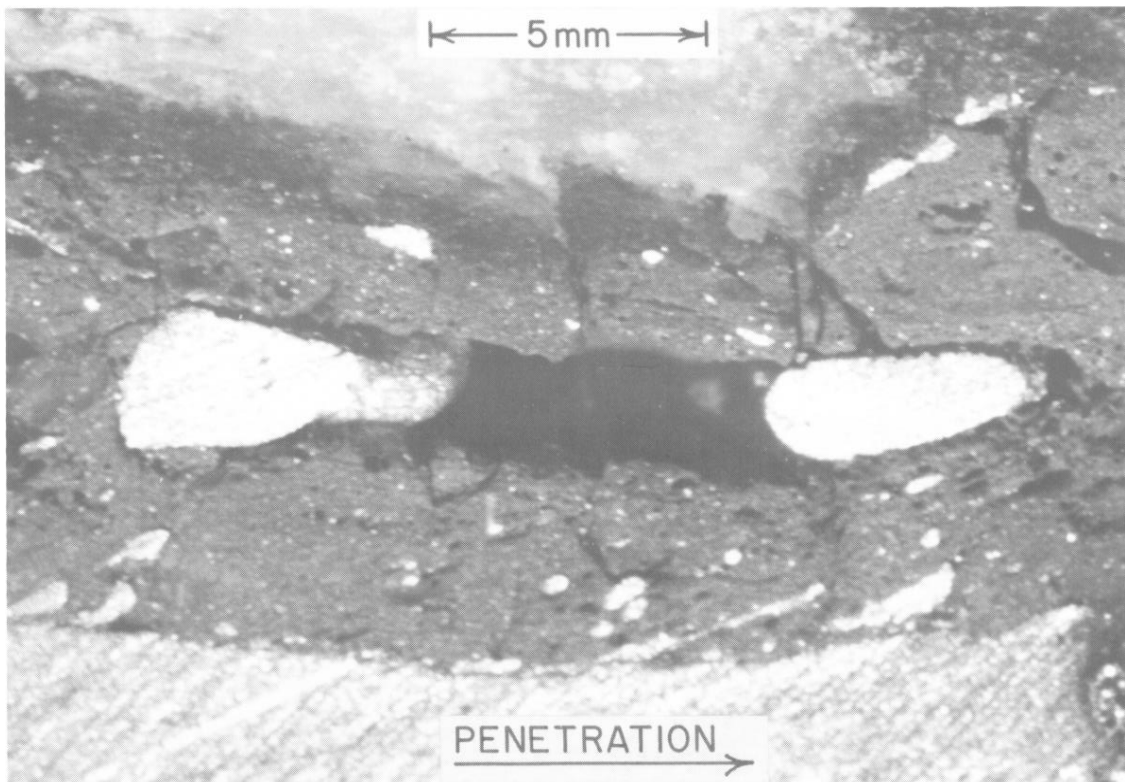
Figure 30. Tapered Jet Particles in Red Glass.

41

2.6 <u>Formation and Role of Red Glass</u>. A recent study by Meade and Jeanloz (1988) was examined for its possible relationship to behavior during jet penetration into glasses. These investigators used a Mao-Bell diamond cell to conduct static high-pressure measurements on a sample of fused quartz mixed with three weight percent ruby of similar particle size. Using ruby fluorescence, they determined both the average pressure and the pressure gradient across the sample, which together with the sample thickness provided an approximate evaluation of the maximum shear stress supported by the sample at pressures between 8.6 and 81 GPa. For convenience, the data of Meade and Jeanloz are plotted in Figure 31. At an average pressure of 8.6 GPa, they concluded that fused quartz flows plastically, with a maximum shear stress less than 1 GPa. This conclusion is consistent with the results of Cagnoux (1981) who concluded from uniaxial strain experiments that a borosilicate glass exhibited plastic response above the dynamic yield stress. Above 8.6 GPa, the maximum shear stress measured by Meade and Jeanloz increased. At 26.9 GPa, it attained a value close to 4.3 GPa, which is approximately the value reported by Proctor, Whitney, and Johnson (1967) at atmospheric pressure where fused quartz undergoes brittle failure. This result is consistent with the result by Anan'in, et al. (1974a), who concluded from shock-wave experiments that fused quartz fails into microblocks separated by interlayers of melt. Similarly, Kanel, Molodets, and Dremin (1976) concluded from shock wave experiments that K-8 glass (a borosilicate composition) fails into particles with the subsequent formation of fused interlayers. Above a pressure of 26.9 GPa, the data of Meade and Jeanloz show that the maximum shear stress decreases to approximately 0.3 GPa at a pressure of 65 GPa.

Interface pressure during the initial part of jet penetration into fused quartz corresponds to average pressures where Meade and Jeanloz reported the highest values of shear strength. This suggests that brittle interface behavior occurs at the penetration front, with the possibility that jet and target materials mix locally and rapidly produce the red glass. This possibility was evaluated experimentally by using the technique of Franz and Lawrence (1987) to remove the rear portion of a copper jet and penetrate a glass target with only a fraction of the jet length. With a 17 mm length of jet, a visual examination of the recovered target detected only metallic copper. With a 39 mm length of jet, red glass was clearly beginning to form and accumulate along the penetration path. It was evident from these tests that red glass does not form rapidly as a result of brittle behavior at the penetration front. Instead, it tends to form gradually and accumulate throughout an extended interval during penetration by a copper jet.
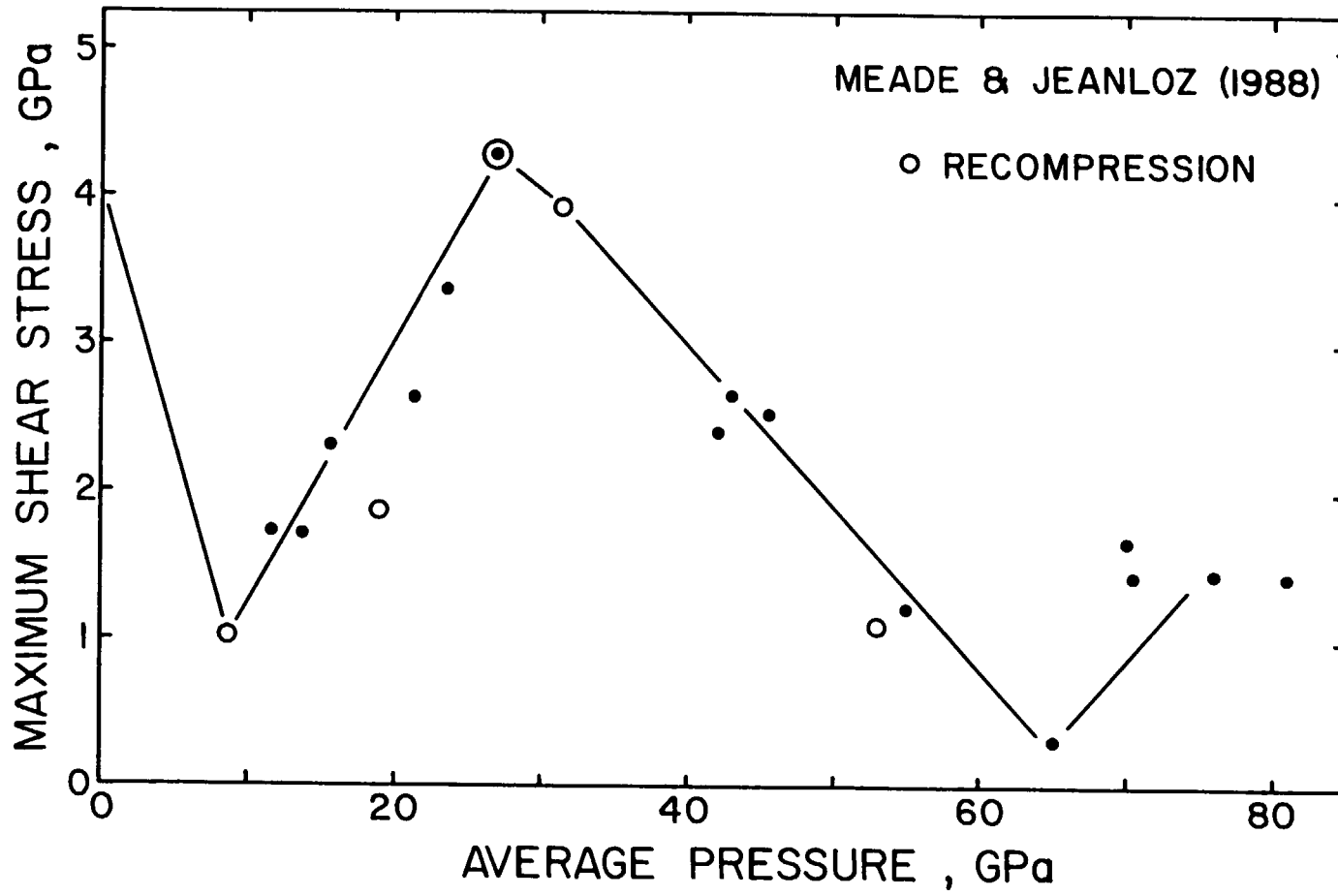
Figure 31. Data of Meade and Jeanloz.

However, the rate of formation may depend on characteristics of the jet/target interaction. Figures 20, 22, and 24 suggest that a glass target may interact more strongly with a jet broken into discrete particles, and it should be noted that the condition of the jet was different in the two tests with a short jet length. With a 17 mm length, 75% of the penetration was by a continuous jet. With a 39 mm length, 99% of the penetration was by discrete particles. The particulated condition of the longer length may have been a factor in the formation of red glass detected in the target recovered form that experiment.

The photographs in Figures 10 and 16 show fine longitudinal detail which suggests the termination of radial cracks at the boundary of the penetration path. The appearance was confirmed when boundary layers were recovered and examined. This observation suggests that opening and closure are accompanied by brittle failure at the cavity wall, producing glass particles which mix with material eroded from the jet. The Modified Bernoulli Penetration Model indicates that erosion products from the jet should flow into the target at a relatively high velocity. In Figure 3, lead-glass tracers show that target material in the penetration path also moves rapidly into the target, implying that it is swept along in the flow of erosion products. The uniform distribution of tracer material in the penetration path implies mixing and an opportunity for target material to interact with the side of the jet. This interaction is confirmed by the abrupt decrease in penetration velocity shortly after closure. Red glass probably is just a by-product of the initial interaction. However, as it accumulates, it must become a major influence of the penetration. Judging by the presence of large jet particles arrested in the red glass, it is highly resistant to penetration. The full role of red glass is not understood at this time, but possible influences are considered in the final discussion.

2.7 <u>Test for Permanent Densification</u>. One recovery experiment was conducted to verify that permanent densification occurs during jet penetration into fused quartz. The configuration of this experiment is shown in Figure 32. The front surface of the fused quartz was unconfined and surrounded by a trap with a small hole to admit the jet. The shaped charge for this test produced a relatively massive and slow moving slug that sealed the hole into the trap. The density of particles recovered from the trap was measured by a procedure similar to the one reported by Wackerle (1962). Dimethyl formamide was floated over methylene iodide in a square cuvette. Slight mixing and diffusion of the two liquids produced a column of varying density which was calibrated by introducing glass particles with different known

44
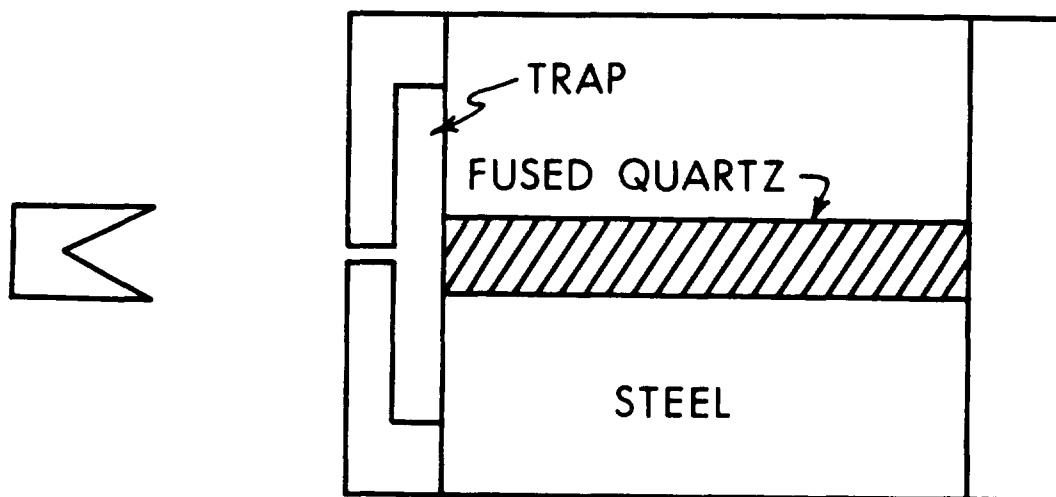
Figure 32. Target Configuration Used to Recover Permanently Densified Fused Quartz.

densities. Recovered particles were also introduced into the column, and particle locations were measured by a traveling microscope at a magnification of 60x. This magnification allowed a careful inspection of each recovered particle to verify that it was not contaminated with copper. Many uncontaminated particles from the trap were found to be permanently densified, and the maximum densification was approximately 10%.

The maximum densification of recovered particles is in close agreement with the results of Arndt, Hornemann, and Muller (1971) who found that maximum permanent densification of 10.37% occurs at a shock stress of 13.5 GPa. However, Cohen and Roy (1965) measured a maximum permanent densification of 19.1% when fused quartz was statically compressed to 15.0 GPa at room temperature. Therefore, the maximum densification during shock loading probably exceeds 10.37%, but the residual temperature anneals and reduces the permanent densification before glass specimens can be recovered for measurements. Highly densified particles were not found in target material surrounding the penetration path in fused quartz. However, annealing at 1,173 K causes almost complete recovery in a few minutes (Arndt, Hornemann, and Muller 1971), and in Figure 28A, remelting around the penetration path in

45

borosilicate glass implies a probable temperature between 1,100 K and 1,500 K. In a fused quartz target, where the diameter of the densified column is less than twice the diameter of the penetration path, heat transfer from the penetration path should produce annealing and explain the absence of particles with a high permanent densification.

2.8 Examination of Recovered Crystalline Quartz Targets. The crystalline quartz target shown in Figure 3B was recovered and examined. A static radiograph of the recovered core is shown in Figure 33A. The slug was not prevented from entering the target and it accumulated in the upper part of the penetration path. The forward flow of jet and tracer material was found in the lower part of the target, with a massive accumulation at the end of penetration. Cross sections from the lower part of the target are shown in Figures 33B–33D. Here, the feathery appearance results from jet material which invaded small radial cracks in the quartz. Cross sections B, C, and D indicate nearly complete closure of the penetration path. There was no evidence that jet penetration into crystalline quartz was influenced by this closure, and this suggests that closure resulted mainly from target material displaced at late times. Factors contributing to this displacement could be the massive accumulation of material at the end of penetration and the slug which was arrested in the preceding section of the target. No red glass was detected in the crystalline quartz target shown in Figure 3B. However, the presence of tantalum carbide may have either influenced the copper/quartz interaction of obscured the presence of red glass. Other crystalline quartz targets were tested either without tracers or with tracers of tantalum metal and were found to contain thin deposits of red glass along the penetration path. This reveals only limited mixing and interaction of the jet and target materials in crystalline quartz and indicates relatively conventional behavior, with interaction only along the cavity wall.

3. SUMMARY AND FINAL DISCUSSION

Experimental studies of jet penetration into glass and crystalline quartz reveal differences that should relate to the ability of these materials to resist penetration. The penetration paths are different, and the jet and target materials interact differently. Permanent densification also distinguishes the behavior of glass from that of crystalline quartz and may have a role in the resistance of glass targets to jet penetration.
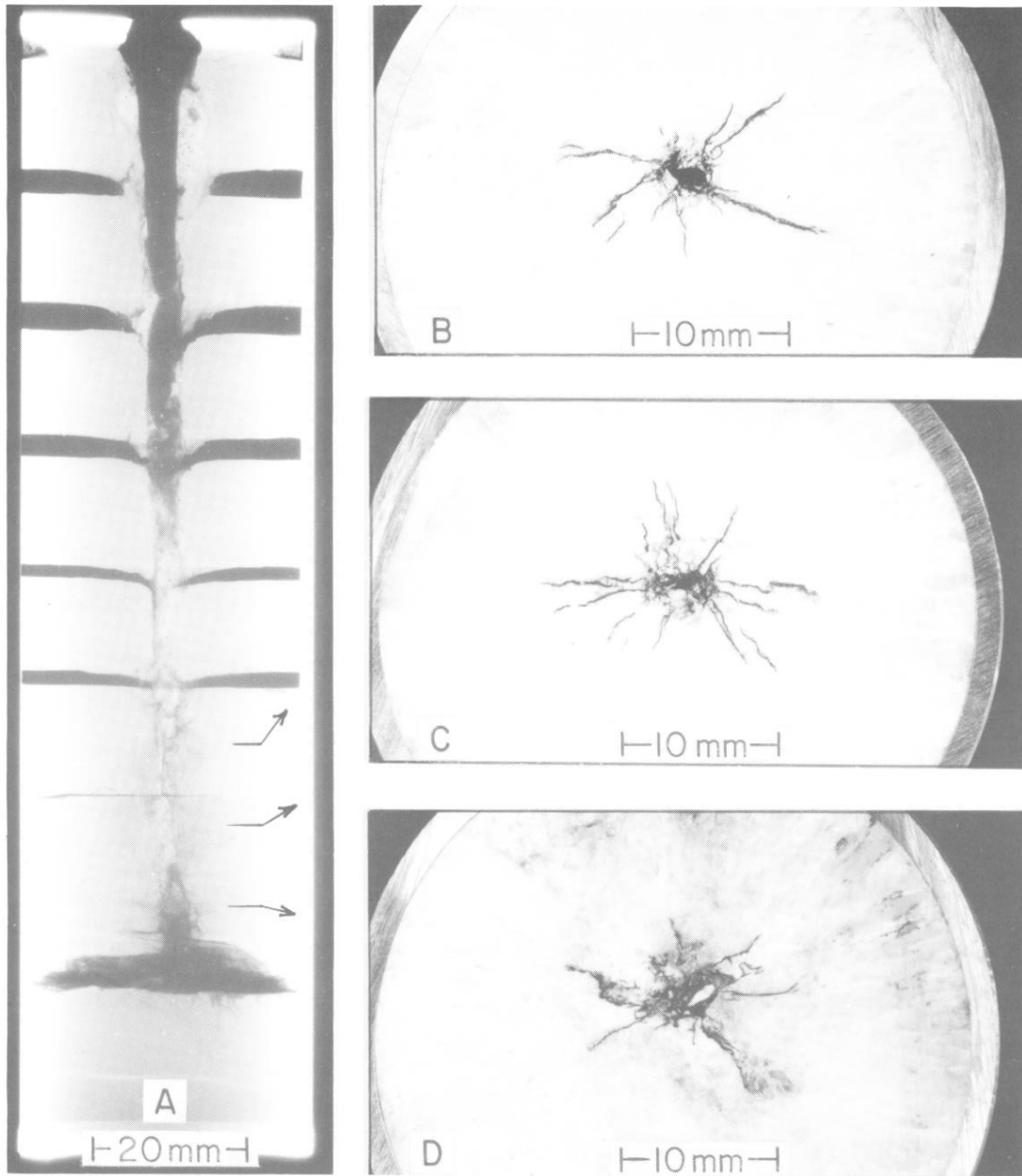
Figure 33. (A) Static Radiograph of the Crystalline Quartz Target; (B–D) Are Cross Sections of the Target in (A) Showing Cavity Closure.

47

The penetration behavior of crystalline quartz is relatively conventional. The jet is surrounded by a cavity and there is only limited mixing of jet and target materials, as indicated by thin deposits of red glass along the penetration path. A recovered target provided evidence of cavity closure, but there was no substantial evidence that closure occurred early in the penetration or that it influenced the penetration into crystalline quartz.

Photographic observations indicated less conventional behavior in glass targets. A small copper jet produces a penetration path which opens to its maximum diameter in a few microseconds and then closes rapidly after the penetration front passes. The boundary of permanently densified glass shows only a slight necking associated with elastic recovery of the surrounding target material. If back-lighted photographs were the only source of information, then the strong refraction of back light by the permanently densified volume might be mistaken for opacity associated with fracture. However, with front lighting, the target is observed to remain transparent in to the boundary of the penetration path where the only evidence of brittle fracture is detected. Unless bubbles are present, no brittle failure is detected within the permanently densified volume or in the surrounding target until damage propagates either from an interface or from the impacted surface. This suggests that initial closure of the penetration path is caused by recovery from high pressures near the penetration front and does not result from dilatancy associated with target failure into discrete particles. Measurements of closure show that the inside diameter of the penetration path approaches the diameter of the jet, producing an interaction which is detected by an abrupt decrease in the penetration velocity (increase in resistance to penetration). Flash radiographs show that the jet is disrupted in a glass target, and it is concluded that path closure is the primary influence.

The boundary of the penetration path in glass exhibits features of brittle failure, and brittle behavior both at peak interface pressures and after pressure release is consistent with data presented in Figure 31. Brittle failure of target material at the boundary of the penetration path is also consistent with the presence of glass particles in the penetration path. Initially, the glass particles must be permanently densified as a result of high pressures experienced at the penetration front. Glass particles accumulate in the penetration path where they interact with the jet and its erosion products. This interaction causes melting of the glass particles and both melting and vaporization of copper jet material. Melting produces a volume recovery of

48

the glass and, together with porosity, enables glass to fill the penetration path. The red color gradually develops as copper becomes suspended and partially reacts with the glass.

Porosity in red glass is tentatively attributed to pockets of vaporized jet material which eventually condenses to coat the surface of pores. Steel jets have been found to produce relatively little porosity in glass that accumulates in the penetration path, and this is consistent with a vaporization temperature higher than that of copper. The greater effectiveness of steel jets against glass targets (Heine-Geldern 1954; Allison 1960) suggests that vaporization and the resulting porosity have an influence on the jet/target interaction.

Material flow in the penetration path is another potential influence on the jet. The penetration model indicates that erosion products, in most cases, flow into glass targets at a high rate. Tracer experiments indicate that local target material accompanies the flow of erosion products. Material flow within an irregular penetration path, as shown in Figure 14, may contribute to disruption of the jet. Layering dissimilar target materials should also produce irregular penetration paths which may be disruptive, especially during oblique penetration.

Although dilatancy associated with brittle failure is not the primary cause of path closure in targets of soda-lime gas, it may make a secondary contribution. When failure occurred at bubbles in a glass target, the early increase in target resistance may have resulted from a contribution of dilatancy to path closure. Also, if dilatancy is able to bulge the front steel confinement of glass targets (the "rebound effect" [Heine-Geldern 1954; Allison 1960]) it may also contribute to jet disruption by opposing reopening of the penetration path which is shown in Figures 14 and 17.

INTENTIONALLY LEFT BLANK.

4. REFERENCES

Allison, F. E. "Defeat of Shaped Charge Weapons." Final report, Contract No. DA-36-061-ORD-507 Carnegie Institute of Technology, Pittsburgh, PA, April 1960.

Anan'in, A. V., O. N. Breusov, A. N. Dremin, S. V. Pershin, A. I. Rogacheva, and V. F. Tatsii. "Action of Shock Waves in Silicon Dioxide II. Quartz Glass." Fizika Goreniya i Vzryva, vol. 10, pp. 578–583, July–August 1974a.

Anan'in, A. V., O. N. Breusov, A. N. Dremin, S. V. Pershin, and V. F. Tatsii. "The Effect of Shock Waves on Silicon Dioxide I. Quartz." Fizika Goreniya i Vzryva, vol. 10, pp. 426–436, May–June 1974b.

Arndt, J., U. Hornemann, and W. F. Muller. "Shock-Wave Densification of Silica Glass." Physics and Chemistry of Glasses, vol. 12, pp. 1–7, February 1971.

Bridgman, P. W., and I. Simon. "Effects of Very High Pressure on Glass." Journal of Applied Physics, vol. 24, pp. 405–413, April 1953.

Cagnoux, J. "Shock-Wave Compression of a Borosilicate Glass Up to 170 kbar." Paper presented at the APS Conference, Stanford Research Institute, Menlo Park, CA, June 1981.

Cohen, H. M., and R. Roy. "Densification of Glass at Very High Pressures." Physics and Chemistry of Glasses, vol. 6, pp. 149–161, October 1965.

Franz, R. E., and W. Lawrence. "Design of a System for Cutting Shaped Charge Jets for Penetration Experiments." BRL-MR-3608, U.S. Army Ballistic Research Laboratory, Aberdeen Proving Ground, MD, June 1987.

Gibbons, R. V., and T. J. Ahrens. "Shock Metamorphism of Silicate Glasses." Journal of Geophysical Research, vol. 76, pp. 5489–5497, August 1971.

Hauver, G. E., and K. A. Benson. "Asymmetry of Detonation Waves Emerging From M36 and M36-M18 Initiated Tetryl Pellets." BRL-MR-893, U.S. Army Ballistic Research Laboratory, Aberdeen Proving Ground, MD, May 1955.

Heine-Geldern, R. V. "Critical Review of Shaped Charge Information: Chapter IX. Defeat of Shaped Charge Weapons." BRL Report 905, U.S. Army Ballistic Research Laboratory, Aberdeen Proving Ground, MD, May 1954.

Kanel, G. I., A. M. Molodets, and A. N. Dremin. "Investigation of Singularities of Glass Strain Under Intense Compression Waves." Fizika Goreniya i Vzryva, vol. 13, pp. 906–912, November–December 1976.

Meade, E., and R. Jeanloz. "Effect of Coordination Change on the Strength of Amorphous Silica." Science, vol. 241, pp. 1072–1074, 26 August 1988.

Meyer, H. W. "Investigation of the Hypersonic Flowfield Surrounding a Shaped Charge Jet." BRL-TR-2883, U.S. Army Ballistic Research Laboratory, Aberdeen Proving Ground, MD, December 1987.

Proctor, B. A., I. Whitney, and J. W. Johnson. "The Strength of Fused Silica." Proceedings of the Royal Society of London Ser. A, vol. 297, pp. 534–557, 21 March 1967.

Pugh, E. M., R. V. Heine-Geldern, S. Foner, and E. Mutschler. "Kerr Cell Photography of High Speed Phenomena." Journal of Applied Physics, vol. 22, pp. 487–493, April 1951.

Sugiura, H., K. Kondo, and A. Sawaoka. "Dynamic Response of Fused Quartz in the Permanent Densification Region." Journal of Applied Physics, vol. 52, pp. 3375–3382, May 1981.

Tate, A. "A Theory for the Deceleration of Long Rods After Impact." Journal of the Mechanics and Physics of Solids, vol. 15, pp. 387–399, 1967.

Tate, A. "Further Results in the Theory of Long Rod Penetration." Journal of the Mechanics and Physics of Solids, vol. 17, pp. 141–150, 1969.

Viard, J. "Hugoniot Curve of Vitreous Silica and Crystallization Under Shock." Comptes Rendus. Academie des Sciences (Paris), vol. 249, pp. 820–822, 1959.

Wackerle, J. "Shock-Wave Compression of Quartz." Journal of Applied Physics, vol. 33, pp. 922–937, March 1962.

Weyl, W. A. Couloured Glasses. Published by the Society of Glass Technology - England, Distributed by State Mutual Book and Periodical Services, NY, 1951.

Zernow, L., D. Garfinkle, D. Buhman, and J. Burchfield. "Final Report on the Evaluation of New Armor Concepts." Report no. 220, Shock Hydrodynamics Inc., Sherman Oaks, CA, April 1975.

Zernow, L., and G. Hauver. "Study of Jet Penetration Into Glass Targets." Shaped Charge Journal, April 1955.

2   Administrator
Defense Technical Info Center
ATTN: DTIC-DDA
Cameron Station
Alexandria, VA 22304-6145

1   Commander
U.S. Army Materiel Command
ATTN: AMCDRA-ST
5001 Eisenhower Avenue
Alexandria, VA 22333-0001

1   Commander
U.S. Army Laboratory Command
ATTN: AMSLC-DL
2800 Powder Mill Road
Adelphi, MD 20783-1145

2   Commander
U.S. Army Armament Research,
  Development, and Engineering Center
ATTN: SMCAR-IMI-I
Picatinny Arsenal, NJ 07806-5000

2   Commander
U.S. Army Armament Research,
  Development, and Engineering Center
ATTN: SMCAR-TDC
Picatinny Arsenal, NJ 07806-5000

1   Director
Benet Weapons Laboratory
U.S. Army Armament Research,
  Development, and Engineering Center
ATTN: SMCAR-CCB-TL
Watervliet, NY 12189-4050

(Unclass. only)1   Commander
U.S. Army Armament, Munitions
  and Chemical Command
ATTN: AMSMC-IMF-L
Rock Island, IL 61299-5000

1   Director
U.S. Army Aviation Research
  and Technology Activity
ATTN: SAVRT-R (Library)
M/S 219-3
Ames Research Center
Moffett Field, CA 94035-1000

1   Commander
U.S. Army Missile Command
ATTN: AMSMI-RD-CS-R (DOC)
Redstone Arsenal, AL 35898-5010

1   Commander
U.S. Army Tank-Automotive Command
ATTN: ASQNC-TAC-DIT (Technical
      Information Center)
Warren, MI 48397-5000

1   Director
U.S. Army TRADOC Analysis Command
ATTN: ATRC-WSR
White Sands Missile Range, NM 88002-5502

1   Commandant
U.S. Army Field Artillery School
ATTN: ATSF-CSI
Ft. Sill, OK 73503-5000

(Class. only)1   Commandant
U.S. Army Infantry School
ATTN: ATSH-CD (Security Mgr.)
Fort Benning, GA 31905-5660

(Unclass. only)1   Commandant
U.S. Army Infantry School
ATTN: ATSH-CD-CSO-OR
Fort Benning, GA 31905-5660

1   Air Force Armament Laboratory
ATTN: WL/MNOI
Eglin AFB, FL 32542-5000

Aberdeen Proving Ground

2   Dir, USAMSAA
ATTN: AMXSY-D
      AMXSY-MP, H. Cohen

1   Cdr, USATECOM
ATTN: AMSTE-TC

3   Cdr, CRDEC, AMCCOM
ATTN: SMCCR-RSP-A
      SMCCR-MU
      SMCCR-MSI

1   Dir, VLAMO
ATTN: AMSLC-VL-D

10   Dir, BRL
ATTN: SLCBR-DD-T

1	Director Central Intelligence Agency ATTN: W. Waltman, OSWR/OSD/GPWB P.O. Box 1925 Main Station Washington, DC 20505
1	Commander U.S. Army Intelligence Agency Foreign Science and Technology Center ATTN: M. Scott Mingledorff 220 Seventh Street, NE Charlottesville, VA 22901-5396
1	U.S. Army Research Office ATTN: Dr. K. Iyer P.O. Box 12211 Research Triangle Park, NC 27709
5	Director U.S. Army Materials Technology Laboratory ATTN: SLCMT-MRD, Dr. G. Bishop Dr. S-C Chou Dr. D. Viechnicki Dr. D. Dandekar Mr. P. Woolsey Arsenal Street Watertown, MA 02172-0001
1	Director Defense Advanced Research Projects Agency ATTN: LTC J. H. Beno 1400 Wilson Blvd. Arlington, VA 22209-2308
1	Air Force Armament Laboratory ATTN: AD/CZL (W. Dyess) Eglin Air Force Base, FL 32542-5000
3	Los Alamos National Laboratory ATTN: Dr. G. E. Cort, MS K574 Dr. R. Karpp, MS P940 Dr. L. M. Hull, MS J960 P.O. Box 1663 Los Alamos, NM 87545

3	Lawrence Livermore National Laboratory ATTN: Dr. L. Glenn, MS L-200 Mr. J. Reaugh, MS L-290 Mr. B. Moran, MS L-200 P.O. Box 808 Livermore, CA 94550
2	Sandia National Laboratories ATTN: Dr. M. J. Forrestal Dr. Dennis Grady P.O. Box 5800 Albuquerque, NM 87185
1	Southwest Research Institute ATTN: Dr. C. E. Anderson, Div. 6 P.O. Drawer 28510 San Antonio, TX 78284
1	California Research & Technology ATTN: Dr. D. Orphal 5117 Johnson Drive Pleasanton, CA 94566
1	General Research Corporation ATTN: Dr. A. Charters 5383 Hollister Avenue Santa Barbara, CA 93160-6770
1	Battelle, Edgewood Operations ATTN: R. Jameson, Suite 200 2113 Emmorton Park Road Edgewood, MD 21040
1	E. I. DuPont DeNemours & Company ATTN: B. Scott Chestnut Run - CR 702 Wilmington, DE 19898
1	Univ. of Dayton Research Inst. ATTN Dr. S. J. Bless Dayton, OH 45469
1	Zernow Technical Services, Inc. ATTN: Dr. Louis Zernow 425 W. Bonita Ave., Suite 208 San Dimas, CA 92121

No. of
Copies Organization

   1   Dr. R. J. Eichelberger
         409 Catherine Street
         Bel Air, MD 21014

   2   Teledyne Brown Engineering
         Armor Technology, Strategic
           Systems Division
         ATTN: Mr. D. L. Puckett
                Dr. D. N. Hansen
         Cummings Research Park
         300 Sparkman Drive, NW
         Huntsville, AL 35807-7007

No. of
Copies Organization

1   Mr. D. E. Finch
     AA4 Division
     RARDE(FH), Sevenoaks
     Kent TN14 7BP, UK

1   Mr. Gerard Solve
     Center D'Etudes de Gramat
     46500 Gramat, France

1   Mr. Patrick Barnier
     Etablissment Technique de Bourges
     Carrefour de Zero - Nord - Route
       de Guerry
     BP712 18015 Bourges Cedex France

1   Dr. U. Hornemann
     Fraunhofer-Institut, EMI
     Institutsteil Weil am Rhein
     Postfach 1270
     D-7858 Weil am Rhein, Germany

1   Dr. Ives Remillieux
     Chef du Departement
     Compartement des Materiaux
     Etablissement Technique Central
       de L'armement
     16 bis Avenue Prieur de la Cote
       d'Or
     94114 Arcueil Cedex France

1   Dr. Florence Tardivel
     Compartment des Materiaux
     Etablissement Technique Central
       de L'armement
     16 bis Avenue Prieur de la Cote
       d'Or
     94114 Arcueil Cedex France

56

USER EVALUATION SHEET/CHANGE OF ADDRESS

This laboratory undertakes a continuing effort to improve the quality of the reports it publishes. Your comments/answers below will aid us in our efforts.

1. Does this report satisfy a need? (Comment on purpose, related project, or other area of interest for which the report will be used.) _____

_____

_____

2. How, specifically, is the report being used? (Information source, design data, procedure, source of ideas, etc.) _____

_____

_____

3. Has the information in this report led to any quantitative savings as far as man-hours or dollars saved, operating costs avoided, or efficiencies achieved, etc? If so, please elaborate. _____

_____

_____

4. General Comments. What do you think should be changed to improve future reports? (Indicate changes to organization, technical content, format, etc.) _____

_____

_____

BRL Report Number _____BRL-TR-3273_____ Division Symbol _____

Check here if desire to be removed from distribution list. ____

Check here for address change. ____

Current address: Organization _____
                  Address _____

_____

NO POSTAGE
NECESSARY
IF MAILED
IN THE
UNITED STATES

BUSINESS REPLY MAIL
FIRST CLASS PERMIT No 0001, APG, MD

Postage will be paid by addressee